The biggest splash

Vasily Belokurov [1]*, Jason L. Sanders [1], Azadeh Fattahi [2], Martin C. Smith,[3]
Alis J. Deason [2], N. Wyn Evans[1] and Robert J. J. Grand [4,5,6]

[1]*Institute of Astronomy, Madingley Rd, Cambridge CB3 0HA, UK*
[2]*Institute for Computational Cosmology, Department of Physics, University of Durham, South Road, Durham DH1 3LE, UK*
[3]*Key Laboratory for Research in Galaxies and Cosmology, Shanghai Astronomical Observatory, Chinese Academy of Sciences, 80 Nandan Road, Shanghai 200030, China*
[4]*Heidelberger Institut für Theoretische Studien, Schloß-Wolfsbrunnenweg 35, D-69118 Heidelberg, Germany*
[5]*Zentrum für Astronomie der Universität Heidelberg, Astronomisches Recheninstitut, Mönchhofstr. 12-14, D-69120 Heidelberg, Germany*
[6]*Max-Planck-Institut für Astrophysik, Karl-Schwarzschild-Str. 1, D-85748 Garching, Germany*

ABSTRACT

Using a large sample of bright nearby stars with accurate *Gaia* Data Release 2 astrometry and auxiliary spectroscopy we map out the properties of the principle Galactic components such as the 'thin' and 'thick' discs and the halo. We confirm previous claims that in the Solar neighbourhood, there exists a large population of metal-rich ([Fe/H] > -0.7) stars on highly eccentric orbits. By studying the evolution of elemental abundances, kinematics, and stellar ages in the plane of azimuthal velocity v_ϕ and metallicity [Fe/H], we demonstrate that this metal-rich halo-like component, which we dub the *Splash*, is linked to the α-rich (or 'thick') disc. Splash stars have little to no angular momentum and many are on retrograde orbits. They are predominantly old, but not as old as the stars deposited into the Milky Way (MW) in the last major merger. We argue, in agreement with several recent studies, that the Splash stars may have been born in the MW's protodisc prior to the massive ancient accretion event which drastically altered their orbits. We cannot, however, rule out other (alternative) formation channels. Taking advantage of the causal connection between the merger and the Splash, we put constraints of the epoch of the last massive accretion event to have finished 9.5 Gyr ago. The link between the local metal-rich and metal-poor retrograde stars is confirmed using a large suite of cutting-edge numerical simulations of the MW's formation.

Key words: Galaxy: formation – Galaxy: halo – galaxies: dwarf – Local Group.

1 INTRODUCTION

Until recently, chronology of the Milky Way's (MW) assembly had been mostly hypothesized, but now it is possible to *determine* the formation history of our Galaxy thanks to data from ESA's *Gaia* space observatory (Gaia Collaboration et al. 2016). By combining *Gaia*'s astrometry with auxiliary spectrophotometry, ages can be measured for increasingly large samples of stars (see e.g. Sanders & Das 2018). Thus, we can now hope to establish the order in which the principal MW components – such as thick and thin discs, bar, bulge, and halo (stellar and dark) – were created. Of these, the chronology of the stellar halo is the simplest to piece together, as the remains of the individual building blocks can stay observable almost indefinitely (Helmi & de Zeeuw 2000). Within the Λ-cold dark matter (ΛCDM) cosmology, the bulk of the stellar halo of a MW-sized galaxy is predicted to be dominated by a small

number of massive early-accreted dwarfs (e.g. Bullock & Johnston 2005; Robertson et al. 2005; Font et al. 2006; De Lucia & Helmi 2008). In connection with this, Deason et al. (2013) put forward the hypothesis that the rapid transition in the Galactic stellar halo structural properties at the so-called break radius of 20–30 kpc (see Watkins et al. 2009; Deason, Belokurov & Evans 2011; Sesar, Jurić & Ivezić 2011) is due to the apocentre pile-up of the tidal debris from a small number of significant mergers early in the life of the MW.

The Deason et al. (2013) hypothesis has recently been tested with the *Gaia* data. Using *Gaia* Data Release 1 (DR1) and the recalibrated Sloan Digital Sky Survey (SDSS) astrometric catalogues, Belokurov et al. (2018) and Myeong et al. (2018b) point out the local dominance of a relatively metal-rich, mildly prograde, and highly radially anisotropic stellar halo component. In fact, the anisotropy is so strong that the local velocity distribution appears highly stretched in the radial direction, taking a cigar- or sausage-like shape. Comparing the *Gaia*-DR1–SDSS data to cosmological zoom-in simulations, Belokurov et al. (2018) argue

* E-mail: vasily@ast.cam.ac.uk

that only massive ($\sim 10^{11}$ M$_\odot$) early (8–11 Gyr ago) mergers can deliver large amounts of stellar material with high orbital anisotropy into the Solar neighbourhood. Similarly, Haywood et al. (2018) use *Gaia* DR2 to contend that the debris from a single significant merger must be the cause of the prominence of stars with high tangential velocity and intermediate metallicity, i.e. [Fe/H] < −1 in the local *Gaia* samples.

Subsequently, the properties of this ancient Gaia-Sausage (GS) merger (sometimes also referred to as Gaia Enceladus) have been further constrained using the *Gaia* DR2 data (GDR2). For example, Helmi et al. (2018) use GDR2 astrometry and APOGEE (Apache Point Observatory Galactic Evolution Experiment) spectroscopy to show that stars on highly eccentric orbits follow a characteristic track in the [α/Fe] and [Fe/H] plane. Note that the first hints of this track were already seen in Meza et al. (2005), who correctly interpreted the available chemokinematics as the undeniable signs of accretion. From the isochronal age of the GS stars, Helmi et al. (2018) estimate the merger to have happened ~ 10 Gyr ago. Mackereth et al. (2019) also look at the APOGEE data, highlighting a tight connection between the chemistry and the orbital properties of the GS stars. By comparing the observed stellar halo chemodynamics to that emerging from the EAGLE (Evolution and Assembly of GaLaxies and their Environments) simulations suite, Mackereth et al. (2019) gauge the stellar mass of the progenitor to be $< 10^9$ M$_\odot$ and the accretion redshift $z \sim 1.5$.

While these original studies presented a broad-brush interpretation of the local stellar halo properties, in the last year there has been plenty of follow-up work that has filled in the missing details. For example, Vincenzo et al. (2019) model the chemical evolution of the GS candidate stars as selected using the APOGEE and GDR2 data sets, and find a total stellar mass at the time of the merger of order of $\sim 10^9$ M$_\odot$, with the bulk of the dwarf's stars forming more than 10 Gyr ago. The presence of the GS merger debris was also revealed through a careful analysis of the local halo sample (Necib, Lisanti & Belokurov 2019b) and traced far beyond the Solar neighbourhood (Bird et al. 2019; Lancaster et al. 2019). Deason et al. (2018) connect the orbital properties of the local main-sequence stars and the distant Blue Horizontal Branch stars and show that the two samples have very similar apocentric distance, thus establishing that the local and the far-field halo tracers likely share a common progenitor. Using independent sets of halo tracers, Wegg, Gerhard & Bieth (2019) and Tian et al. (2019) confirm that the GS debris has a small but statistically significant prograde rotation in agreement with Deason et al. (2017), Belokurov et al. (2018), and Myeong et al. (2018b). Myeong et al. (2019) present chemical and kinematic evidence for two (perhaps related) accretion events: the nearly radial GS merger (see Belokurov et al. 2018) and the highly retrograde Sequoia (see also Myeong et al. 2018a; Matsuno, Aoki & Suda 2019). The structural properties of the GS debris cloud were mapped out in Iorio & Belokurov (2019), who demonstrate that the bulk of the RR Lyrae stars within 20-30 kpc were probably once part of the GS progenitor galaxy. According to Iorio & Belokurov (2019), the inner halo RR Lyrae distribution is triaxial, with the major axis almost in the Magellanic Cloud orbital plane. Curiously, at either end of this triaxial ellipsoid there reside two previously known halo substructures: the Virgo Overdensity and the Hercules-Aquila Cloud. Simion, Belokurov & Koposov (2019) make a compelling case that both VO and HAC are likely unmixed portions of the GS tidal debris.

Globular clusters (GCs) can provide a unique window into the early accretion history of the Galaxy. Several studies took advantage of the fast growing number of GCs with accurate ages and

kinematics to produce independent constraints on the early merger events in the MW. In a pioneering study, Kruijssen et al. (2019) claim to have identified three significant early mergers, although note that their assignment of individual GCs to particular events does not use any orbital information. Myeong et al. (2018c) complemented the sample provided by Kruijssen et al. (2019) with the GC orbital properties from Gaia Collaboration et al. (2018c) to discover a large group of clusters likely originating from the GS dwarf galaxy (see also Piatti & Carballo-Bello 2019), thus confirming the high mass of the progenitor. Myeong et al. (2019) refine the GS membership probability for the Galactic GCs (see also Massari, Koppelman & Helmi 2019) and estimate the dwarf's total stellar mass of up to 5×10^9 M$_\odot$ prior to its disruption in the MW. Note that most recently, Deason, Belokurov & Sanders (2019) came up with a direct measurement of the total Galactic stellar halo mass using the *Gaia* DR2 kinematics. Their value of $\sim 10^9$ M$_\odot$ is in good agreement with the above indirect estimates.

There have also been several attempts to compare the observational evidence for an early massive merger with the numerical simulations of the MW's formation. Looking in the Aquarius simulation suite, Fernández-Alvar et al. (2019a) see a variety of accretion pathways imprinted in the distinct alpha-iron abundance trends as a function of Galactocentric radius, albeit without a clear match to the MW observations described above. Mackereth et al. (2019) identify counterparts of the observed local high-eccentricity stars in the EAGLE suite of cosmological zoom-in simulations. Complementing their study with [Mg/Fe]–[Fe/H] information, they arrive at the stellar mass of the progenitor galaxy of the order of 10^9 M$_\odot$. Fattahi et al. (2019) take a different approach, attempting to reconstruct the details of the merger by comparing the observed properties of the local stellar halo to those of the simulated Auriga galaxies (see Grand et al. 2017, for details). Following Belokurov et al. (2018), Fattahi et al. (2019) model the local velocity distribution with a mixture of multivariate Gaussians and find that those Auriga haloes that contain a dominant velocity component with an orbital anisotropy $\beta > 0.8$ are typically assembled early, undergoing a merger with Large/Small Magellanic Cloud-sized dwarf galaxy 6–11 Gyr ago.

Note however that, in numerical simulations of galaxy formation, stellar haloes are typically assembled through at least two distinct channels. In mock MWs, stars at large distances from the Galactic plane (following a loose definition of a halo) can be either accreted from smaller satellites (see e.g. Johnston, Hernquist & Bolte 1996; Helmi & White 1999; Bullock & Johnston 2005; Cooper et al. 2010) or born *in situ* (Zolotov et al. 2009; McCarthy et al. 2012; Tissera, White & Scannapieco 2012; Cooper et al. 2015). The details of the *in situ* halo formation differ between the above studies. In the most recent revision of the problem, Cooper et al. (2015) list three different channels of *in situ* stellar halo formation. Curiously, according to Cooper et al. (2015), the protodisc heating provides the smallest contribution to the *in situ* halo, but can dominate in the Solar neighbourhood with a caveat that an unambiguous distinction between the thick disc and the *in situ* halo in this region may be difficult. Interestingly, they also see *in situ* halo star formation (SF) directly from gas particles accreted on to the MW. This can be either smoothly accreted gas of the gas stripped from gas-rich satellites. Cooper et al. (2015) caution however that this mode of SF may be an artefact of the subgrid physics prescriptions used in the simulations.

A search for an *in situ* stellar halo component has been on for some time now. It is however clear from the discussion above that depending on the formation scenario, the present-day *in situ* stellar haloes can have drastically different properties. Zolotov et al. (2009) and McCarthy et al. (2012) agree that the *in situ* component

ought to be old and metal-rich, while forecasting rather different kinematics: in one case, *in situ* haloes do not have to have any appreciable angular momentum while in the other, they typically maintain significant net rotation. On the other hand, if stars can be born in the halo from the gas stripped from gas-rich dwarfs (as suggested by Cooper et al. 2015), at redshift $z = 0$, such an *in situ* component will have properties indistinguishable from that of the accreted halo. Some authors took the observation by Carollo et al. (2010) that the MW stellar halo evolves from metal-rich at small Galactocentric radii to metal-poor further out as evidence for the presence of an *in situ* stellar halo in the inner Galaxy. It is however becoming increasingly clear that the metal-rich ([Fe/H] ~ -1.6) 'inner halo' identified by Carollo et al. (2010) is nothing but the tidal debris from the ancient GS merger, whose extent is largely limited to 20–30 kpc (see Deason et al. 2013, 2018).

The question of the existence of the Galactic *in situ* stellar halo has been revived in light of the recent *Gaia* DRs. Using the *Gaia* DR1 data augmented with the RAVE (RAdial Velocity Experiment) and APOGEE spectroscopy, Bonaca et al. (2017) build a large sample of high-eccentricity stars with [Fe/H] > -1. Using the available chemical information and by comparing their observations to numerical simulations, Bonaca et al. (2017) conclude that these locally observed metal-rich stars on halo-like orbits have likely been born *in situ*. They estimate that this *in situ* component contributes as much as 50 per cent of the halo stars locally. Haywood et al. (2018), Di Matteo et al. (2018), and Amarante, Smith & Boeche (2019) use *Gaia* DR2 to detect a substantial (again close to ~ 50 per cent) population of high-eccentricity stars with thick disc chemistry, in agreement with the *Gaia* DR1 study of Bonaca et al. (2017). These authors choose not to label this component an '*in situ* halo' but rather a 'heated thick disc', perhaps in line with the earlier definition of the *in situ* halo Zolotov et al. (see e.g. 2009). Note however that the *in situ* stellar halo is defined explicitly as a heated pre-historic disc in the works of McCarthy et al. (2012) and Cooper et al. (2015). Gallart et al. (2019) provide a fresh new evidence for the existence of *in situ* halo. They concentrate on the split main sequence discovered by Gaia Collaboration et al. (2018b) and claim that the stars analysed by Bonaca et al. (2017), Haywood et al. (2018), Di Matteo et al. (2018) and earlier by Nissen & Schuster (2010), Nissen & Schuster (2011), and Schuster et al. (2012) are typically as old as the oldest accreted halo stars and significantly older than the bulk of the thick disc population.

In this paper, we study chemo-chronological properties of a large sample of stars on halo-like orbits, i.e. those with low or no angular momentum. Our focus is on the metal-rich, more precisely $-1 <$ [Fe/H] < 0 portion of this population, which we demonstrate to be clearly distinct from the accreted (and typically more metal-poor) stars of the GS. We show that at the same metallicity, there exists a smooth transition from this low-angular momentum population to the rapidly rotating 'thin' and 'thick' discs. We introduce our data set in Section 2 and highlight the differences between the metal-poor and metal-rich halo components in Section 3. We extend out analysis beyond the Solar neighbourhood in Section 4. Finally, in Section 5, the observations are compared to numerical simulations of the MW's formation. We also invoke virial theorem to provide an analytic estimate of the mass of the massive perturber based on the energetics of the encounter.

2 A GLIMPSE OF THE GALAXY IN 9D

Our primary dataset is based on the large sample of nearby stars with accurate *Gaia* DR2 (Gaia Collaboration et al. 2018a)

astrometry and auxiliary spectroscopy, augmented with 2MASS (Two Micron All Sky Survey, Skrutskie et al. 2006), *Gaia*, and Pan-STARRS (Panoramic Survey Telescope and Rapid Response System, Magnier et al. 2013) photometry as produced by Sanders & Das (2018). In particular, spectroscopic information from the APOGEE (Majewski et al. 2017; García Pérez et al. 2016) DR14 (Abolfathi et al. 2018), LAMOST DR3 (Large Sky Area Multi-Object Fibre Spectroscopic Telescope, Cui et al. 2012; Zhao et al. 2012), RAVE (Steinmetz et al. 2006) DR5 (Kunder et al. 2017), *Gaia*-ESO DR3 (Gilmore et al. 2012), GALAH (GALactic Archaeology with HERMES, De Silva et al. 2015; Martell et al. 2017) DR2 (Buder et al. 2018), and SEGUE (Sloan Extension for Galactic Understanding and Exploration, Yanny et al. 2009) surveys is included. The data were compared to a grid of PARSEC isochrone models (Bressan et al. 2012; Chen et al. 2014; Tang et al. 2014; Chen et al. 2015) in a probabilistic sense. For giant stars with carbon and nitrogen measurements, constraints on the mass were also used using the method of Das & Sanders (2019). Not only do Sanders & Das (2018) use the extant spectroscopic information to constrain their distance estimates and measure stellar ages, they also re-calculate stellar atmosphere parameters, thus unifying the spectroscopic output across all surveys considered. There are three features of the Sanders & Das (2018) method worth mentioning: (i) the maximum age isochrone considered is 12.6 Gyr, (ii) there is a weak prior coupling 3D location in the Galaxy, age, and metallicity, and (iii) no offset was applied to the *Gaia* parallaxes as its magnitude for the sample was, at the time, not well characterized. The impact of the latter of these is somewhat alleviated by also using spectrophotometric information, although recent studies (e.g. Schönrich, McMillan & Eyer 2019) have shown the offset for bright stars, such as those in the spectroscopic overlap, is significantly greater than for the quasar sample from Lindegren et al. (2018). This will be discussed in more detail later.

Given that there exist substantial overlaps between the above surveys, we restrict the sample to the subset of stars with unique *Gaia* source_id. From the Sanders & Das (2018) catalogue of 49 06 746 (37 06 733) entries including (excluding) duplicates we select unique objects with a small azimuthal velocity error $\sigma_{v_\phi} < 20$ km s^{-1} and low metallicity uncertainty $\sigma_{[Fe/H]} < 0.15$ as well as accurate parallax measurement $|\varpi/\sigma_\varpi| > 5$. The above cuts leave the total of 26 55 034 stars available. Additionally, when considering alpha-abundance, we also require $\sigma_{\alpha/Fe} < 0.1$, which reduces the sample down to 8 15 930. Our sample is diminished from 26 55 034 down to 5 14 286 when the stellar ages are analysed, in particular we set $\sigma_{age} < 4$ Gyr and only include upper main-sequence and turn-off stars (MSTO), i.e. those with 5700 K $< T_{eff} <$ 8300 K and 3.5 $<$ log $g <$ 4.3. The stellar velocity components as well as the orbital properties discussed below are those reported in the catalogue of Sanders & Das (2018).

Fig. 1 shows the distribution of stars in the space of (cylindrical) azimuthal velocity v_ϕ and metallicity [Fe/H] (as derived by Sanders & Das 2018). Only stars between 0.5 and 3 kpc away from the Galactic plane are shown, which reduces the sample size by a factor of ~ 3. As is clear from the first panel in this grid (top left), there exists a small yet noticeable population of metal-rich ([Fe/H] > -1) stars with no appreciable angular momentum, i.e. $v_\phi < 100$ km s^{-1}. Strikingly, many of these stars are on radial ($v_\phi \sim 0$ km s^{-1}) and some are on retrograde ($v_\phi < 0$ km s^{-1}) orbits in agreement with previous studies (in particular Bonaca et al. 2017; Haywood et al. 2018; Di Matteo et al. 2018). The next panel in the top row presents the column-normalized density which allows one to track the peak of v_ϕ distribution as a function of [Fe/H].
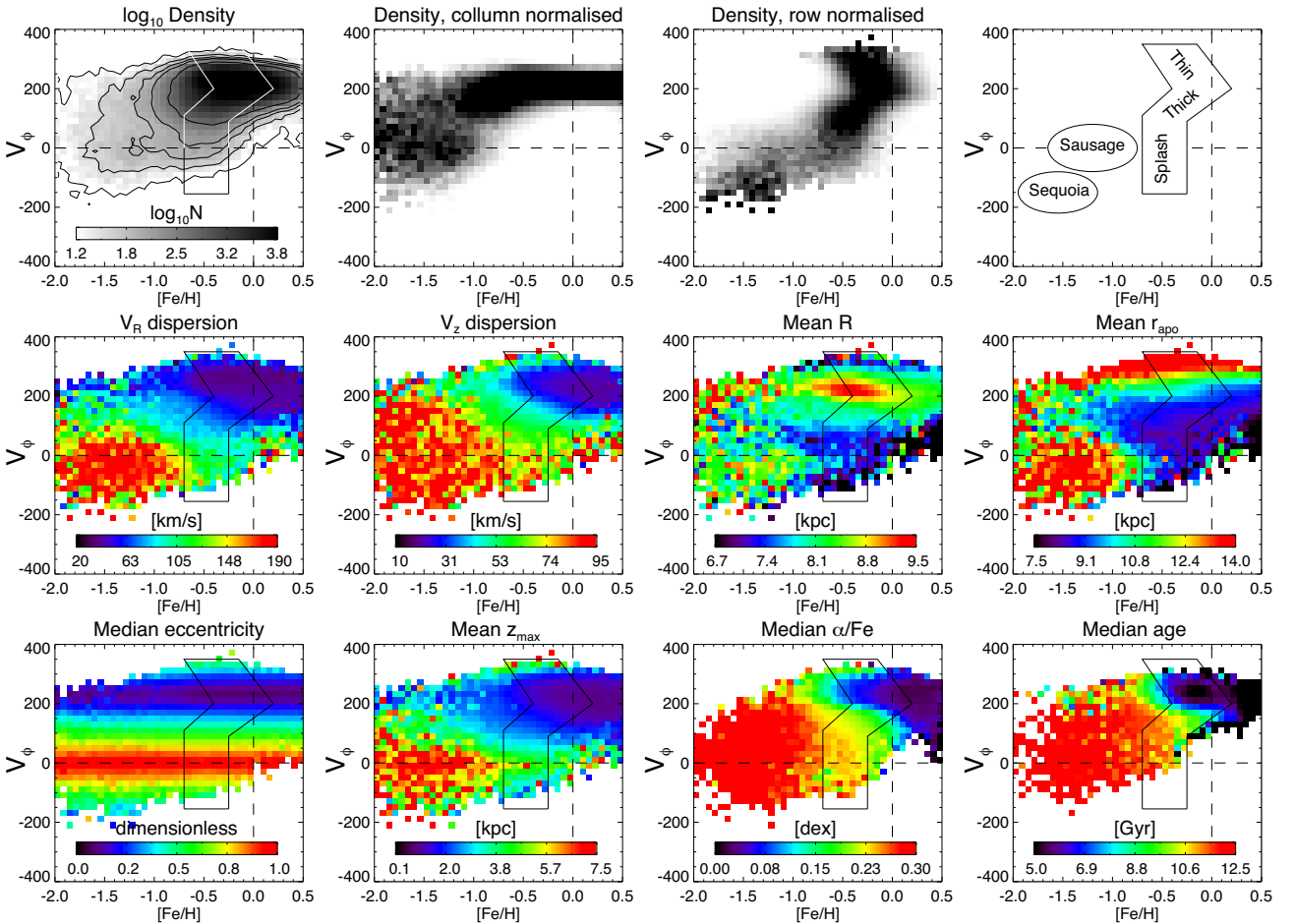
Figure 1. Stars with $0.5 < |z|\text{(kpc)} < 3$ in the plane of v_ϕ-[Fe/H]. Top row: first panel shows the logarithm of the stellar density. Second panel gives column-normalized stellar density. Note the bimodality in the v_ϕ distribution at $-1.5 <$ [Fe/H]< -0.7, where the high v_ϕ population is the Galactic disc, and low v_ϕ population is the GS. Third panel shows the row-normalized stellar density. Note the chevron-like $>$ pattern of the thin and thick discs (see the text for details) as well as the very metal-rich population with low and/or negative v_ϕ. Fourth panel presents a schematic summary of the feature seen in the previous panels. Middle row: first panel shows the radial velocity dispersion. Note a clear dichotomy between the accreted halo with [Fe/H] < -1 and $v_\phi < 100$ km s^{-1} seen in red here and the Galactic discs with [Fe/H] > -1 and $v_\phi > 100$ km s^{-1} seen in blue. The Splash stars (mostly green) with $-0.7 <$ [Fe/H]-0.2 and $v_\phi < 100$ km s^{-1} have radial velocity dispersion significantly higher than that of the disc but lower than the GS. Second panel gives the vertical velocity dispersion. Third: mean instantaneous cylindrical radius. Compared to GS stars, the Splash is preferentially observed inside of the Solar radius. Fourth panel: mean apocentric distance. Note a clear difference between the GS and Splash stars. Bottom row: first panels gives the median eccentricity. All stars with $v_\phi < 100$ km s^{-1} have $e > 0.5$. Second: mean z_{max}. Note a transition to much larger heights at $v_\phi \sim 100$ km s^{-1} and $-0.7 <$ [Fe/H] < -0.2. Third: median α-abundance. The Splash [α/Fe] ratios are the highest at the corresponding metallicity and overlap with low-v_ϕ tail of the thick disc. Fourth: median stellar age. The Splash stars are slightly younger than those in GS and overlap with the old age (and low v_ϕ) tail of the thick disc.

Here, at the intermediate metallicity of [Fe/H] ~ -1.3 two distinct modes can be seen, one with $v_\phi \sim 150$ km s^{-1} corresponding to the thick disc and one with $v_\phi \sim 0$ km s^{-1} corresponding to the stellar halo, more precisely to its dominant local component, the GS (see Belokurov et al. 2018). The third panel in the top row of Fig. 1 shows the row-normalized density in the space of v_ϕ and [Fe/H], which reveals the typical metallicity for the given range of azimuthal velocity. Starting from the highest values of v_ϕ and going down, a bifurcated chevron-like $>$-sign feature is discernible, corresponding to the 'thin' (upper portion of $>$) and 'thick' (lower portion of $>$) discs (see also Lee et al. 2011). The 'thin' disc stars show negative v_ϕ gradient as a function of metallicity. This behaviour arises in the Solar neighbourhood for the same reason as the so-called asymmetric drift. Stars with higher v_ϕ are those for which their motion on the epicyclic ellipse adds to the motion of the guiding centre – such stars have to come from Galactocentric

radii larger than Solar. Given the negative metallicity gradient in the Galactic disc, these faster stars are also more metal-poor. The 'thick' disc shows an inverted v_ϕ–metallicity gradient. This is a manifestation of the so-called Simpson–Yule paradox and is the consequence of the inside-out disc formation (see Schönrich & Mcmillan 2017; Kawata et al. 2018; Minchev et al. 2019).

At $v_\phi \sim 0$ km s^{-1}, the density runs without clear interruptions across almost the entire range of metallicities. Note however, that the number of stars with low or negative v_ϕ drops quickly at [Fe/H] > -0.2. At large negative velocities, i.e. $v_\phi < -100$ km s^{-1}, an over-density with $-2 <$ [Fe/H] < -1.3 is visible, corresponding most likely to the debris from the so-called Sequoia event (see Myeong et al. 2019). Finally, the fourth and the last panels in the top row gives the schematic representation of the main features described above. The boundaries of the 'thick' and 'thin' disc sequences wrap tightly around the chevron $>$-sign feature seen in the previous panel, while

the ellipses marking the locations of the two main ancient accretion event are more approximate. Finally, a vertical rectangular box marks the boundaries of a section of the v_ϕ, [Fe/H] space designated as 'Splash'. The Splash stars have $-0.7 <$ [Fe/H] < -0.2. This box's metal-rich boundary corresponds to the metallicity where the number of stars with retrograde velocities quickly drops (see first and third panels in the top row). The rationale for choosing the metal-poor boundary $-0.7 <$ [Fe/H] is laid out below.

The middle row of Fig. 1 presents the orbital properties of the stars in our sample. The disc and the accreted halo populations have demonstrably distinct colours in most panels of this row. For example, the disc stars have large azimuthal velocities and low radial (first panel) and vertical (second panel) dispersions. The majority of stars with low azimuthal velocities $v_\phi < 100$ km s^{-1} and low metallicity ([Fe/H] < -1) possess much higher velocity dispersions and clearly belong to the accreted halo. Note however, that moving from low [Fe/H] towards higher [Fe/H] at constant $v_\phi \sim 0$ km s^{-1}, the bulk kinematics change dramatically around [Fe/H] ~ -0.7. For example, as shown in the first panel of the middle row of the figure, the radial velocity dispersion drops here from $\sim$180 to $\sim$110 km s^{-1}. Similarly, the vertical velocity dispersion drops from $\sim$80 to $\sim$60 km s^{-1}; these changes imply a smaller radial and vertical extent. This clear switch in the kinematics at [Fe/H] $\sim = -0.7$ motivates our choice of the low-metallicity boundary for the population we have designated the 'Splash'.

Note that this boundary demarcates not only stars with different kinematics, but also distinct orbital properties. As seen in the fourth panel in the middle row, the orbits of metal-poor stars with low angular momentum can reach Galactocentric radii of $\sim$15 kpc. Stars with higher [Fe/H], on the other hand, tend to turn around at $\sim$9 kpc, in agreement with the radial velocity behaviour described above. The fact that the Splash stars are more centrally concentrated is also supported by the distribution of the instantaneous radial positions shown in the third panel of the middle row. Here, the typical value for the GS stars is $\sim$8 kpc, i.e. the Solar radius and the centre of our selection box, implies that their radial scale length is much larger than the extent of our sample. The metal-rich Splash population on the other hand, is typically found inside the Solar radius with $R \sim 7$ kpc.

The bottom row of Fig. 1 strengthens the view that the Splash stars are subtly different from both the Galactic halo in general and the GS, as well as the Galactic 'thick' and 'thin' discs. As indicated by the first panel, while the orbital eccentricities of the bulk of the disc stars is $e < 0.3$, the metal-rich low-angular-momentum stars have $e > 0.5$, with many objects at $e \sim 1$. In the Solar neighbourhood, probed by the Sanders & Das (2018) sample, the Splash stars have typically lower $z_{max} \sim 4$ kpc (the peak Galactic height), compared to the stars with [Fe/H] < -0.7 that on average can reach $z_{max} \sim 8$ kpc. There exists a clear distinction in terms of detailed chemical abundances (third panel) and ages (fourth panel). The majority of the metal-poor halo stars have high [α/Fe] abundance ratios, typically with [α/Fe] > 0.3. Only at $-0.9 <$ [Fe/H] < -0.7, the median [α/Fe] of the GS starts to decrease, diminishing slightly to 0.2–0.25 in agreement with Helmi et al. (2018) and Mackereth et al. (2019). It is not surprising that compared to the typical accreted halo stars, the median [α/Fe] of the Splash stars is lower at [α/Fe] ~ 0.25 given their higher metallicity. It is none the less instructive to compare the [α/Fe] of the Splash stars to those of the disc. At fixed metallicity, the Splash stars have higher [α/Fe], indicating the prevalence of the older stars in this population. The switch in [α/Fe] happens around $v_\phi \sim 100$ km s^{-1}, i.e. at the lower boundary of the thick disc box and the upper boundary of the Splash box. The fourth and final panel in the bottom row of Fig. 1 shows the median age

distribution. The stellar halo hosts the oldest stars in the Galaxy with age >12 Gyr. This can be compared to the thin disc ages that are predominantly lower than $\sim$6 Gyr. The thick disc shows a strong age gradient as a function of v_ϕ in agreement with the picture presented in Schönrich & Mcmillan (2017), Kawata et al. (2018), and Minchev et al. (2019). The metal-rich low-angular-momentum Splash population is slightly younger than the bulk of the stellar halo and is typically as old as the oldest stars in the thick disc.

3 THE HALO AND THE SPLASH

3.1 Velocity ellipsoids

The velocity ellipsoids of the halo-like stars in the GS and the Splash components can be measured using a Gaussian mixture model of the entire velocity distribution (see Belokurov et al. 2018, for details). Fig. 2 presents the projections of the observed velocity ellipsoids on to the $v_\phi - v_R$ plane together with our three-component models. We give the best-fitting model parameters in Table 1. The difference between the velocity ellipsoids of the Splash (top) and the Sausage (bottom) are evident already in the (first) left-hand column of the figure. The second column shows the 2D distribution of the model residuals (reported in numbers of Poisson sigmas). Curiously, even for the very metal-rich disc-dominated sample shown in the top row (stars with $2 < z < 3$ and $-0.7 <$ [Fe/H] -0.2), the three-component Gaussian model does a reasonable job, in particular around $v_\phi \sim 0$ km s^{-1} as can also be seen in the fourth (right) column of the figure. Note that this particular range of Galactic heights is chosen to minimize the number of disc stars and thus increase the relative contribution of the Splash component. 1D v_ϕ projections of the data and the model are shown in the third column. The 'thin' ('thick') disc components are shown with dashed–dotted (dashed) lines. There is a pronounced 'knee' in the observed v_ϕ distribution around $v_\phi \sim 0$ km s^{-1} indicating a need for an additional component. The additional Splash component is shown with a light-blue solid line. When fitting, we fix the mean v_ϕ of the Splash component at different trial values and choose the solution which delivers well-behaved residuals for $v_\phi < 100$ km s^{-1} (see the top right panel of Fig. 2). This procedure yields a mean $v_\phi = 25$ km s^{-1} for the Splash.

The bottom row of Fig. 2 gives the results of the velocity distribution modelling for the stars with $1 < z < 3$ and $-1.5 <$ [Fe/H] < -1. An even stronger 'knee' can be seen in the third panel, corresponding to the GS stars (light-blue solid line in the third panel). The residual distributions shown in the second and fourth panels are much more well behaved since our Gaussian mixture does not need to reproduce the complicated (and non-Gaussian) disc kinematics. Between the top and the bottom rows, there is one Gaussian component in common, namely that corresponding to the 'thick' disc. Re-assuringly, we recover virtually identical 'thick' disc Gaussian parameters as indicated by the blue dashed line shown in the third column of the figure. The third (very low-amplitude) Gaussian here is the nearly isotropic 'other halo' component shown with purple dashed–dotted line. For the performance of the models with a more realistic description of the disc contribution, please see Amarante et al. (2019).

From Table 1, we see that, for $2 < z < 3$ and $-0.7 <$ [Fe/H] < -0.2, the Splash only contributes 7 per cent of all stars. This can be compared to the GS component, which provides 50 per cent of all stars with $1 < z < 3$ and $-1.5 <$ [Fe/H] < -1. However, taking into account the total number of objects in either subsample, the Splash population is almost as numerous as the Sausage (notwithstanding the differences in the Galactic height convolved with the catalogue
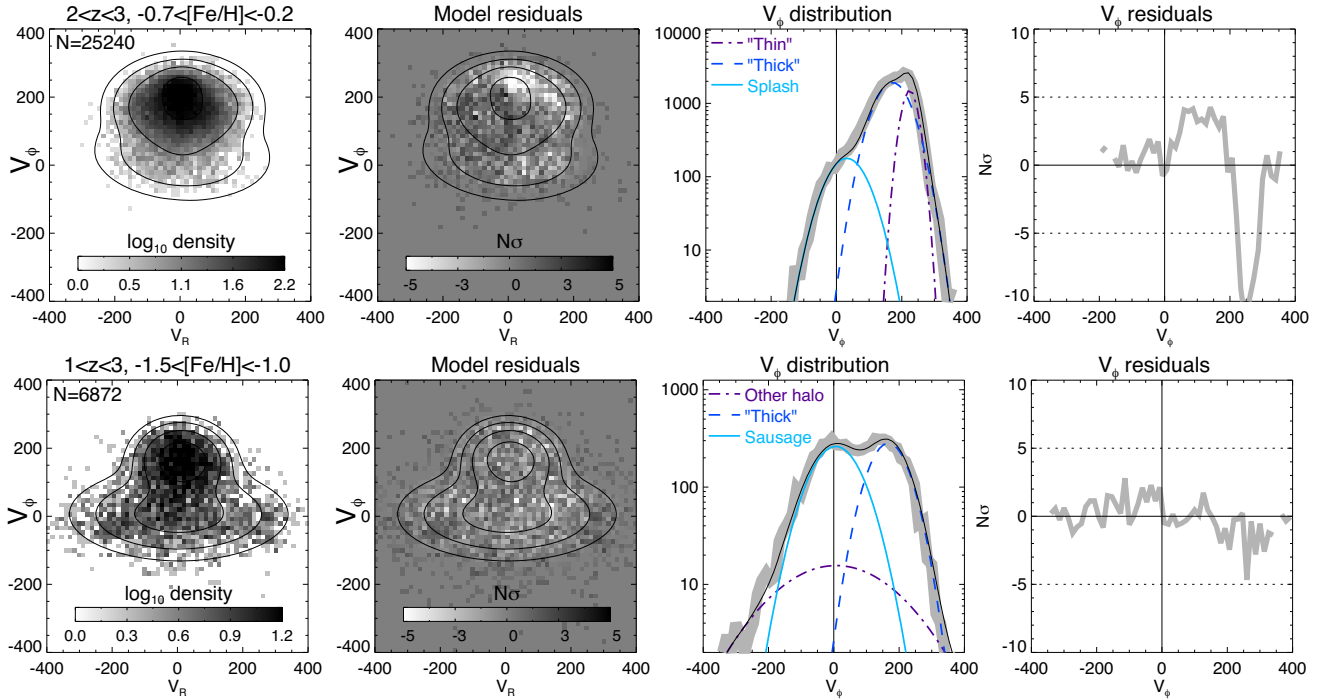
Figure 2. The Splash (top) and the Sausage (bottom) in velocity space. First panel: grey-scale density shows the observed distribution of stars in $v_\phi - v_R$ space. Black contours show the three-component Gaussian mixture model. Second panel: distribution of the model residuals reported as numbers of Poisson sigmas. Third panel: histogram of the observed v_ϕ velocities (thick grey line) together with model (solid thin black line) and three individual components (explained in the legend). Fourth panel: distribution of the model residuals as a function of v_ϕ. Dotted lines show $\pm 5\sigma$. Note that in the top row, unsurprisingly, our oversimplified model does not describe the disc properties adequately (high residuals for $v_\phi > 100$ km s^{-1}. None the less, around $v_\phi \sim 0$ km s^{-1} the model and the data agree well allowing us to estimate the properties of the Splash population.

Table 1. Properties of the Gaussian mixture components.

Component	Fraction (per cent)	$<v_\phi>$ (km s^{-1})	σ_R (km s^{-1})	σ_ϕ (km s^{-1})	σ_Z (km s^{-1})
$2 < |z|$ (kpc)< 3 and $-0.7 < $ [Fe/H] < -0.2					
'Thin'	25	220	31 ± 6	21 ± 4	26 ± 5
'Thick'	68	165	73 ± 7	47 ± 6	48 ± 6
'Splash'	7	25	108 ± 19	54 ± 11	79 ± 21
$1 < |z|$ (kpc) < 3 and $-1.5 < $ [Fe/H] < -1					
'Thick'	42.5	160	73 ± 14	54 ± 9	64 ± 14
'Sausage'	50	0	175 ± 26	68 ± 15	82 ± 13
'Halo'	7.5	0	190 ± 50	164 ± 50	160 ± 50

selection effects). In terms of the radial and vertical velocity dispersions, the Splash is hotter by some ~ 30 km s^{-1} compared to the thick disc, but has an identical (within the uncertainties) azimuthal velocity dispersion of $\sigma_\phi \sim 50$ km s^{-1}. Compared to the GS stars, the radial velocity dispersion is some ~ 75 km s^{-1} smaller but the vertical velocity dispersion is similar at $\sigma_Z \sim 80$ km s^{-1}.

3.2 The angular momentum of the last major merger

The outcome of the collision between the progenitor of the GS and the proto-Galaxy should depend sensitively on the geometry of the interaction. While, most probably, the dwarf's orbit evolved rapidly under the effects of dynamical friction, we can glean the final state of the impactor's angular momentum by measuring the spin of the dominant stellar halo component. The multi-Gaussian velocity field decomposition described above yields $v_\phi \sim 0$ km

s^{-1} for the Sausage component, implying no appreciable angular momentum for the last major debris as measured in the data set of Sanders & Das (2018). This can be compared with the small but statistically significant rotation of ~ 20–30 km s^{-1} reported by Belokurov et al. (2018) using a dataset with a similar reach, i.e. a few kpc from the Sun. This estimate based on the SDSS–Gaia-DR1 data set was recently confirmed by Tian et al. (2019) using nearby LAMOST K-giants in the *Gaia* DR2. On much larger scale, namely tens of kpc throughout the Galaxy, the net stellar halo rotation was measured by Deason et al. (2017) who used three different tracers samples, namely RR Lyrae, Blue Horizontal Branch stars and K giants to arrive at a $v_\phi \sim 15$ km s^{-1}. This is in agreement with the more recent study of the RR Lyrae kinematics carried out by Wegg et al. (2019).

The above studies are clearly at odds with the claim of Helmi et al. (2018) of a strongly retrograde motion of the bulk of the stellar halo locally. Note that this is not the first detection of a retrograde stellar halo motion: for instance, Carollo et al. (2007) measure a small pro-grade rotation for the 'inner halo' but report a net retrograde motion for the 'outer halo' component (also see references to the earlier studies in their work). However according to Schönrich, Asplund & Casagrande (2011), this apparent retrograde spin may largely be due to overestimated distances. Note that it is now established with certainty that the *Gaia* DR2 parallaxes are biased low, implying that the distances are overestimated. For example, Lindegren et al. (2018) report a bias of -0.029 mas from quasars, but warned that the offset could be dependent on on-sky position, magnitude, and colour. Schönrich et al. (2019) measure a stronger bias of -0.054 mas with a small uncertainty (in agreement with Zinn et al. 2019) for the Gaia RVS (Radial Velocity Spectrometer) sample. Moreover
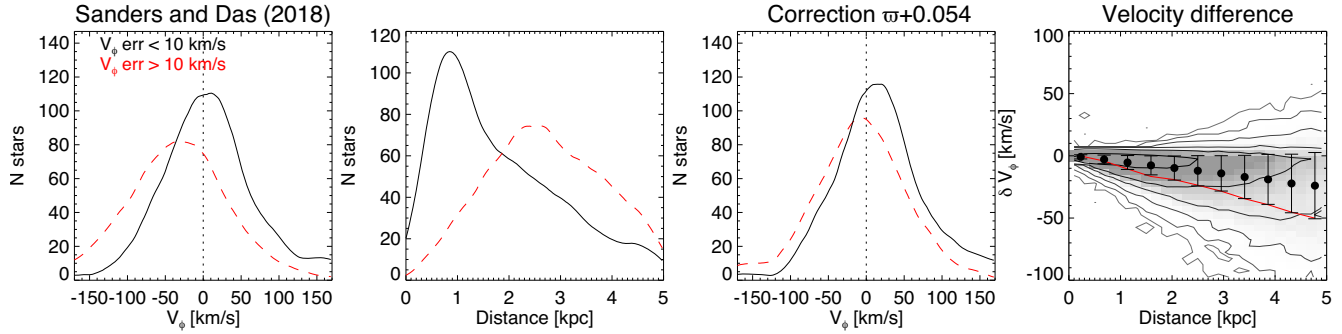
Figure 3. Mean azimuthal velocity of stars with large radial motion. Apart from the conditions described in Section 2 only stars with $-2 <$ [Fe/H] < -0.7, $0 < |z|$ (kpc) < 3 and, most importantly, $|v_R| > 250$ km s^{-1} are shown. Black (red) solid (dashed) lines show the distributions for stars with low (high) v_ϕ uncertainty. Note that for the latter we remove the v_ϕ error <20 km s^{-1} constraint. First panel: v_ϕ distributions obtained with Kernel Density Estimation (with optimal smoothing parameter) employing Epanechnikov kernel (see e.g. Koposov et al. 2011). Note the strong disagreement between the low-uncertainty (small positive $\bar{v}_\phi$) and high-uncertainty (clearly negative $\bar{v}_\phi$) samples. Second panel: heliocentric distance distributions for the low- and high-uncertainty samples. The high-uncertainty sample is dominated by stars with large distances. Third panel: v_ϕ distributions after applying the $\varpi + 0.054$ mas correction advocated by Schönrich et al. (2019). Note that most of the retrograde motion seen in the first panel has vanished and the two distributions show much better agreement. Fourth panel: azimuthal velocity difference $v_\phi - v_\phi^{\varpi+0.054}$ as a function if distance. Overestimating stellar distances leads to a pronounced retrograde bias, which rapidly increases with distance. Data points with error bars show the mean bias and its standard deviation in the given distance bin. Red curve gives the mean v_ϕ bias for stars with v_ϕ error >10 km s^{-1}.

they discover the dependence of the parallax offset on the parallax error, thus exacerbating the bias for distant stars. Sanders & Das (2018) did not apply an offset before deriving output parallaxes from the combination of astrometry and spectrophotometry. As we will see, when the spectrophotometry is highly informative the bias from the astrometry will have a weak effect, but for more uncertain spectrophotometry the output distances (and hence velocities) will inherit the *Gaia* biases. Due to this complex interaction between the different data sources, it is impossible to accurately correct a posteriori for a given parallax offset.

Given the high radial anisotropy of the Sausage stellar debris (see bottom left panel of Fig. 2), it is possible to estimate the bulk angular momentum of this halo component simply by selecting stars with high $|v_R|$. Accordingly, Fig. 3 shows the distribution of azimuthal velocities for the stars in our main sample (see above) but limited to $-2 <$ [Fe/H] < -0.7, $0 < |z|$ (kpc)< 3 and, most importantly, $|v_R| > 250$ km s^{-1}. Additionally, we split this sample into two parts of approximately the same size ($\sim$1200 stars in each): one with small v_ϕ errors <10 km s^{-1} (black solid lines) and one with v_ϕ errors in excess of 10 km s^{-1} (red dashed lines). As evidenced by the figure, the mean spin of the two samples is unmistakably different: the peak of the low-uncertainty sample is at around $+10$ km s^{-1}, while the high-uncertainty distribution peaks at approximately -40 km s^{-1}. The cause of such a drastic difference is hinted at in the second panel of Fig. 3 which shows the heliocentric distance distributions of the two samples. The low-uncertainty sample is largely limited to the nearby stars with distances of order of 1–2 kpc. The high-uncertainty sample is composed of stars with a median distance of $\sim$3 kpc. Note that in accordance with our base selection, all of these stars have $|\varpi/\sigma_\varpi| > 5$ (see Section 2).

Schönrich et al. (2019) use the procedures described in Schönrich, Binney & Asplund (2012) and Schönrich & Aumer (2017) to create a large sample of unbiased distance estimates based on the *Gaia* DR2 parallaxes for the RVS sample. Here, we only use one of the components of their method, namely the global parallax correction of 0.054 mas to investigate the changes in the mean angular momentum of the GS. The results of increasing parallax by 0.054 mas are shown in the third panel of Fig. 3. The distribution of the azimuthal velocities in the low-uncertainty sample shows a small shift towards higher mean prograde motion, with its peak

now at $\sim+20$ km s^{-1}. The v_ϕ distribution of the high-uncertainty sample exhibits a much more dramatic evolution on applying the parallax correction. The distribution tightens up and the peak moves to ~-10 km s^{-1}, displaying overall much better agreement with the low-uncertainty sample. As illustrated in the fourth panel of the figure, the principle cause of the difference in the behaviour of the two samples is the distance-dependent v_ϕ bias caused by using underestimated *Gaia* DR2 parallaxes. According to the distribution of $v_\phi - v_\phi^{\varpi+0.054}$, stars at 3 kpc from the Sun typically display -15 km s^{-1} spurious retrograde motion. Note however, that for stars with large v_ϕ errors (red line) this bias is twice as large -30 km s^{-1} at 3 kpc, and the tails of the distribution reach -100 km s^{-1}. The observed bias is likely larger than that shown in the fourth panel of Fig. 3 as the parallax systematics appear to correlate with the parallax errors (see Schönrich et al. 2019).

Therefore, we conclude that the net retrograde motion of the radially anisotropic local sample claimed by Helmi et al. (2018) is limited to the stars with larger azimuthal velocity uncertainties and may be caused by overestimated distances. We demonstrate that even without accounting for the parallax bias, but limiting the sample to high-accuracy v_ϕ measurements from the Sanders & Das (2018) catalogue, one obtains mean $v_\phi \sim +10$ km s^{-1} for the GS debris. On including the correction, this estimate shifts slightly to $v_\phi \sim +20$ km s^{-1}.

3.3 Dating the last major merger with the Splash

In the metallicity range of the Splash, there appears to be a wide range of ages and angular momenta, not necessarily captured adequately by the median distribution shown in Fig. 1. Accordingly, Fig. 4 explores further correlations between the angular momentum and age for stars with $-0.7 <$ [Fe/H] < -0.2. Note that as described earlier, we apply an additional stellar population restriction for the age study, namely selecting only stars around the MSTO. The figure presents row-normalized density in the space of v_ϕ and age, which allows us to track the typical age for a given range of azimuthal velocity. As clear from the left-hand panel of the figure, for $v_\phi >$ 150 km s^{-1}, a wide range of ages is plausible, highlighting the fact that the SF started in the disc as early as 12 Gyr and proceeded to the present day.
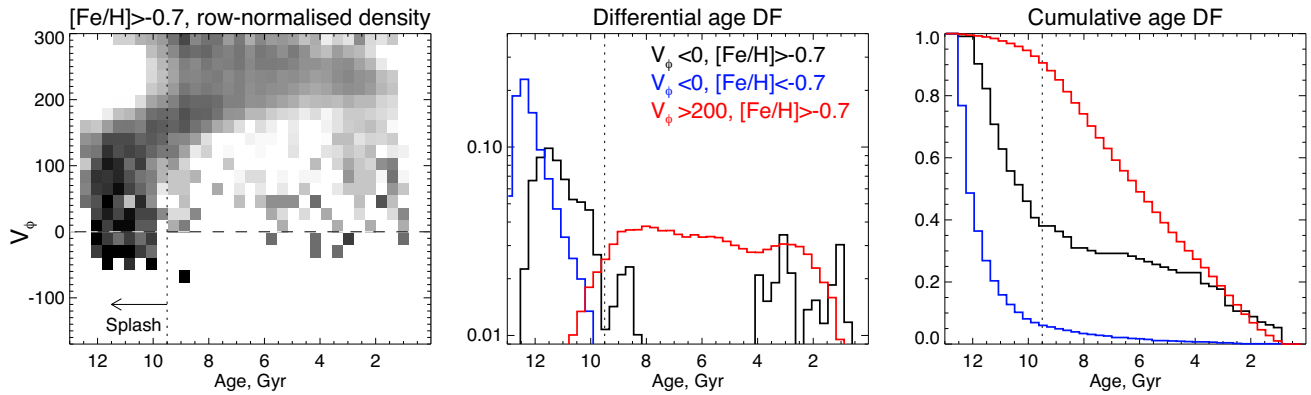
Figure 4. Left: azimuthal velocity of the metal-rich stars $-0.7 <$ [Fe/H] < -0.2 as a function of their age. Note that the retrograde stars are predominantly found with ages between 12.5 and 9.5 Gyr. These $v_\phi < 0$ km s^{-1} stars are found at the base of a vertical overdensity of stars corresponding to the Splash. This low angular momentum population connects seamlessly to the disc at $v_\phi > 100$ km s^{-1}. Middle: age distributions of the Sausage (blue), the Splash (black), and the disc (red). The major merger debris pile-up against the age grid boundary at 12.5, while the heated disc stars peak 1–2 Gyr later. Although the shapes of the age distributions are different, both are truncated at around 9.5 Gyr, which we posit marks the end of the Sausage merger. Right: the cumulative age distributions. Note a clear inflection at 9.5 in both the black (Splash) and blue (GS) lines.

The age distribution for the slower rotating stars, i.e. those with $v_\phi < 150$ km s^{-1} is clearly very different. In particular, the metal-rich retrograde (those with $v_\phi < 0$ km s^{-1}) stars are predominantly found with ages greater than 9.5 Gyr. In the left-hand panel of Fig. 4, these retrograde stars are at the base of an extended column-like feature which stretches over a wide range of azimuthal velocities, from $v_\phi \sim -100$ to $v_\phi \sim +150$ km s^{-1} in the relatively narrow range of ages from 9.5 to 12.5 Gyr. This dark vertical band of stars with $v_\phi < 100$ km s^{-1} and old ages is the Splash. From this figure, the close connection between the Splash and the disc is immediately apparent: it is not clear where the disc stops and the Splash begins. The two clearly overlap at $100 < v_\phi/$kms$^{-1} < 150$. Additionally, as evidenced from the figure, Splash stars display net prograde rotation, albeit with a lower amplitude than the disc.

Given the seamless transition from the disc to the Splash population observed in the left-hand panel of Fig. 4 as well as in the multiple panels of Fig. 1, we hypothesize that Splash is the population of stars originally born in the protodisc of the Galaxy and subsequently kicked (splashed) into low-angular-momentum (high eccentricity) orbits by an accretion event that finished around 9.5 Gyr ago. The best candidate for such an event is the GS merger. We compare the age make-up of the heated disc stars and that of the accreted Sausage stars in the middle panel of Fig. 4. We limit the Splash stars to those with $v_\phi < 0$ km s^{-1} to minimize any disc contamination. The accreted stars are also selected to have $v_\phi < 0$ km s^{-1} but are more metal-poor than [Fe/H] $= -0.7$ (see Fig. 1 for reference). The accreted stars are dominated by the oldest stars in our sample, with the distribution function quickly dropping as a function of formation epoch, with no clear signal discernible younger than 9.5 Gyr. The Splash age distribution looks sufficiently different from that of the GS. For example, its peak is not at 12.5 Gyr but 1 Gyr later, which is understandable as even for something as massive as the MW progenitor, it takes a non-trivial amount of time to self-enrich to [Fe/H] ~ -0.5. Even though the shapes of the age distribution of the Sausage and Splash stars are rather different, they have one particular feature in common: a truncation at 9.5 Gyr.

We thus use the synchronicity between the cessation of SF in the GS and the finishing of the disc heating in the MW to put constraint on the epoch of the last major merger event.

4 SPLASH BEYOND THE SOLAR NEIGHBOURHOOD

The implications of the detection of a large number of stars with [Fe/H] > -0.7 on highly eccentric and relatively energetic orbits in the Solar neighbourhood are clear: there ought to be a corresponding population of metal-rich stars at large Galactocentric radii and heights. In what follows, we first explore the evolution of the density ratio of the metal-poor and metal-rich low-angular-momentum stars in our primary sample (described above) and then probe the existence of such a population using the SDSS and LAMOST K-giant stars.

4.1 Metal-rich to metal-poor density ratio

The parent catalogue of Sanders & Das (2018) comprises data from several spectroscopic surveys, each with its own strong selection effects. These biases are predominantly spatial, driven by each survey's footprint and limiting magnitude. Here, we do not attempt to correct for the strong selection biases affecting our sample. Instead, we assume that these biases impact the metal-rich and the metal-poor stars equally. If this conjecture is correct, the ratio of the metal-rich and metal-poor star counts may be able to reveal the intrinsic evolution of the density of the Splash stars normalized by that of the halo. Note that in the volume probed by our sample, the metal-poor halo population is dominated by the GS debris, which has a triaxial 3D shape (see Iorio & Belokurov 2019) and a characteristic density break around 20–30 kpc from the centre of the Galaxy (see Deason et al. 2018).

Fig. 5 shows the density of metal-poor (first column) and metal-rich (second column) stars in the plane spanned by azimuthal velocity v_ϕ as a function of Galactocentric radius (top) and Galactic height $|z|$ (bottom). As clear from the figure, both radial and vertical density distributions are affected by the selection effects. However, the ratio of the density distributions shown in the third column evolves much more smoothly revealing a particular behaviour of the Splash stars in comparison to the halo population. In the Solar neighbourhood, the ratio of the number of the metal-rich retrograde stars to that of the metal-poor ones is close to 1: 1. It evolves slowly as a function of Galactocentric radius R, dropping to 1:10 at $R \sim$
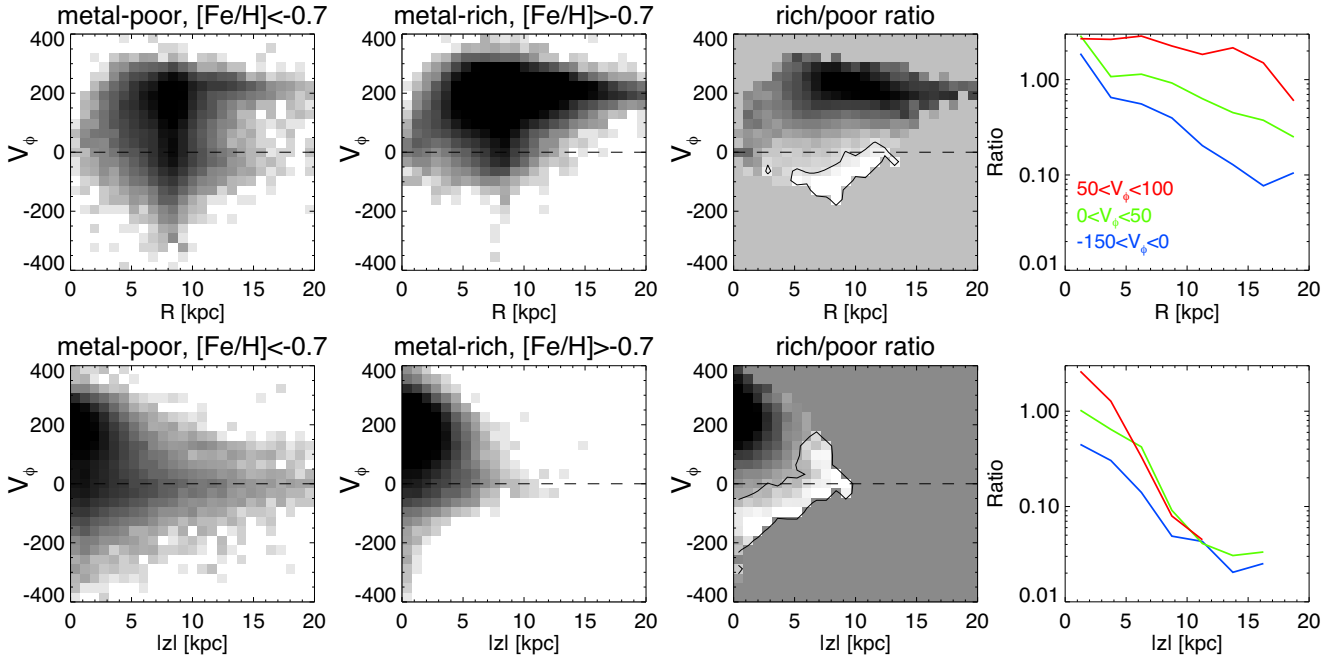
Figure 5. Metal-poor and metal-rich stars in the plane of v_ϕ versus R (top) and $|z|$ (bottom). Note that while our sample is dominated by nearby stars, a small number of objects spans a wide range of R and $|z|$. The selection effects are strong and increase with distance. However we hypothesize that they affect in equal measure the metal-poor (first column) and the metal-rich (second column) sample. Thus, their ratio (third column) may show the true intrinsic variation of the density ratio as a function of R and $|z|$. Note that the overlaid contour in the third panel corresponds to 50 per cent ratio of metal-rich to metal-poor star counts. The fourth column displays the evolution of the density ratio for stars in three v_ϕ bins, starting with purely retrograde (blue), through low net rotation (green) to prograde (red). As clear from both the third and the fourth columnz, the Splash population decays much faster with Galactic height and at $|z| \sim$ 10 kpc drops to a meagre ~ 5 per cent of the halo density.

15 kpc. Vertically, the density ratio evolves noticeably faster, hitting 10 per cent at ~ 7 kpc and ~ 5 per cent around 10–15 kpc.

If the behaviour displayed in the third and fourth columns of Fig. 5 is not seriously affected by the selection effects, we can conclude that the extent (both radial and vertical) of the Splash is considerably smaller than that of the halo. Splash may be limited to 15–20 kpc in the radial direction and 10–15 kpc above the plane.

4.2 The SDSS K-giants

We use the sample of K-giants identified in the SDSS spectroscopy by Xue et al. (2014) who also provide distance estimates to these stars. Out of ~ 6000 objects, only ~ 280 have [Fe/H] > -0.7. Additionally, we also require the metallicity error to be lower than 0.2 and the azimuthal velocity error to be lower than 30 km s^{-1}. We take care to minimize the contamination of our distant Splash sample by the tidal debris from the currently disrupting Sgr dwarf. More specifically, we classify the stars with $|B_{\text{Sgr}}| < 15°$ and heliocentric distance $D > 15$ kpc as those belonging to the Sgr stream. Here, B_{Sgr} is the latitude in the coordinate system aligned with the Sgr's tidal tails, namely a great circle with a pole at (RA, Dec.) = (303.63°, 59.58°) (see e.g. Belokurov et al. 2014). There are 94 likely Sgr stream members with [Fe/H] > -0.7. Finally, to select stars with low angular momentum we require $v_\phi < 100$ km s^{-1}. After applying the above cuts, we end up with 39 metal-rich likely Splash K-giants at large distances from the Sun. We compare these to the disc stars, selected with the same metallicity cut but $v_\phi > 100$ km s^{-1} (96 stars in total) and the halo objects (likely dominated by the GS debris),

identified as those with $v_\phi < 100$ km s^{-1} and $-2 <$ [Fe/H] < -0.7 (1091 stars in total).

Fig. 6 shows the spatial properties of the Splash K-giants (black points and black solid lines) and those in the disc (red points and red dotted lines) and the halo (blue points and blue dashed lines). As the top row of the figure demonstrates, the disc stars are limited to $|z| < 5$ kpc, while the Splash population extends as far as $|z| \sim 20$ kpc. This is not surprising given the findings of Sections 2 and 3. Similarly, in agreement with the local kinematics, the halo populations extend beyond the reach of the Splash stars, i.e. to $|z| > 30$ kpc. In terms of the radial reach, displayed in the bottom row of the figure, the Splash stars can travel as far as $R \sim 25$ kpc, but their R distribution peaks at smaller distances from the Galactic centre compared to both the disc and the halo. Curiously, the radial distance distributions of the disc and the halo are nearly identical as probed by this K-giant sample.

We emphasize that, notwithstanding the low numbers of tracers, the ranking of the vertical and the radial sizes of the Splash, the disc and the halo, i.e. $z_{\text{disc}} < z_{\text{Splash}} < z_{\text{halo}}$ and $R_{\text{Splash}} < R_{\text{halo}}$, is likely robust to the selection biases of the SDSS K-giant sample. Supporting evidence can be found in Fig. 7 which compares the Galactocentric positions of the Splash and disc populations to those of the Sgr stream members (yellow points). Sgr stars are chosen using the same metallicity cut as the Splash and the disc, i.e. [Fe/H] > -0.7. As the figure clearly demonstrates, the SDSS K-giant sample contains plenty of metal-rich and distant stars, i.e those with $r > 25$ kpc (all in the Sgr stream). Yet, the Splash giants are mostly limited to $r < 20$ kpc, with more than a half of our sample at $r < 15$ kpc.
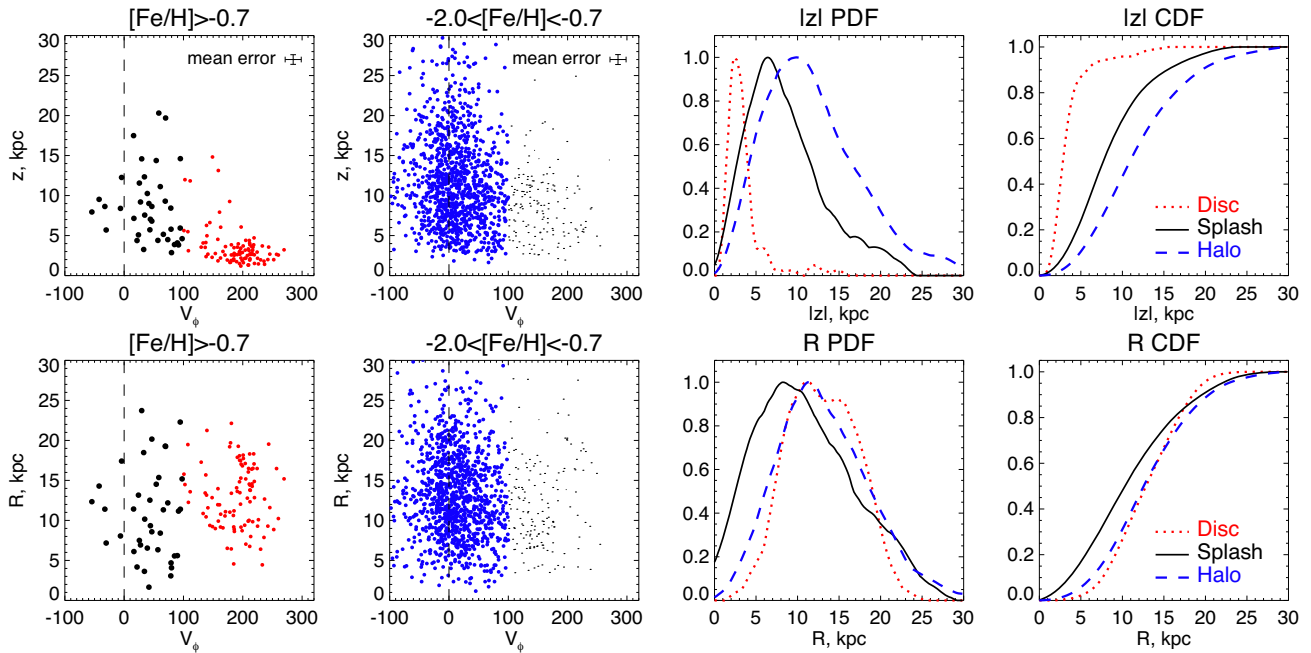
Figure 6. SDSS K-giants in the Splash (black, solid), disc (red, dotted), and halo (blue, dashed). All distributions are obtained using Kernel Density Estimation with Epanechnikov kernel and optimal scale. Top row: $|z|$ distributions. First panel: $|z|$ versus azimuthal velocity v_ϕ for stars with [Fe/H] > -0.7. Second panel: same as previous panel but for stars with $-2 <$ [Fe/H] < -0.7. Third panel: probability distributions for the three populations selected as shown in the first two panels. The disc extent is smaller than that of the Splash, which in turn is not as large as that of the halo. Fourth panel: cumulative distributions. Bottom panel: R distributions. Panels are the same as above but for R instead of $|z|$. As the third and the fourth panels demonstrate, the radial size of the Splash is smaller that that of the disc and the halo, which match each other in 2D projected distance as traced by the SDSS K-giants.
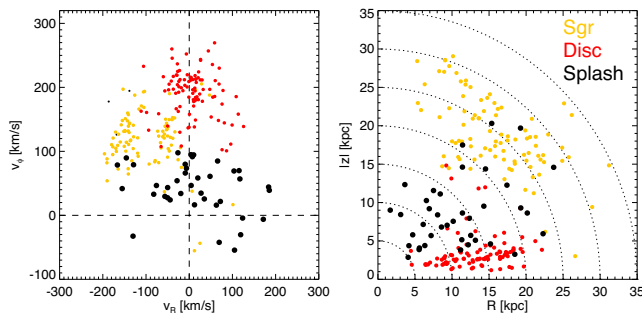
Figure 7. Metal-rich K-giants in the Sgr tidal stream (yellow) are compared to those in the Splash and the disc. Sgr K-giants are selected to have the same metallicity, but can clearly be seen extending much further in $|z|$ and/or R.

Overall, the behaviour of the SDSS K-giants support conclusions of the previous subsection. The Splash stars amount to only $3 - 5$ per cent of the halo density at these large Galactic radii and heights. The extent of the Splash is much smaller than that of the halo: its reach is curbed around 15–20 kpc in R and 10–15 kpc in $|z|$. The peak of the Splash's R (z) distribution function is at 10 (7) kpc.

4.3 The LAMOST K-giants

In order to increase our sample size, we now explore a larger catalogue of K-giants from the LAMOST survey (Luo et al. 2015). This is constructed using stellar parameters from the SP_Ace pipeline (Boeche et al. 2018), which has been updated using the fifth LAMOST DR. We use stars where SP_Ace has converged

without any errors, the SP_Ace signal-to-noise ratio is greater than 20, $|b| > 10$ deg and the following error cuts: $\delta\log(g) < 0.5$, $\delta T_{eff} <$ 150 K, δ[Fe/H] < 0.15 dex, $\delta v_R < 30$ km s^{-1}, $\delta\mu_\alpha < 0.5$ mas yr^{-1}, and $\delta\mu_\delta < 0.5$ mas yr^{-1} are satisfied. We also reject stars observed prior to MJD $= 55945$ as these have been shown to be problematic (see Boeche et al. 2018). Duplicates have been removed, retaining only the spectrum with highest signal-to-noise ratio. Our K-giants are selected using a cut of $\log(g) < 3.4$ and $T_{eff} < 5600$ K. To ensure we have minimal contamination from late-type dwarfs we have imposed a further cut of $M_G < 3$, where M_G is calculated from the parallax and for all stars we require parallax error to be less than 0.2 arcsec. Although this parallax error cut likely removes some low signal-to-noise bona fide giants, we feel that this is warranted so as to give us as clean a sample of giants as possible.

For the stars with parallax error less than 20 per cent the distance has been calculated by inverting the parallax. For those with parallax error greater than 20 per cent distances have been calculated using a random forest regression tool trained on a high-quality subset of the data with parallax errors less than 15 per cent $\delta\log(g) < 0.2$, $\delta T_{eff} < 100$ K, δ[Fe/H] < 0.1 dex, $|b| > 30$ deg, and $|z| > 0.5$ kpc. The penultimate cut minimizes the importance of the extinction correction and the final cut is used to avoid the regression being dominated by thin disc stars. For most of these stars the distance accuracy is around 15 per cent, although for the brightest stars ($M_G < -2$) the errors increase and so we have excluded these from our analysis. For all LAMOST giants, the extinction correction is derived from the maps of Schlegel, Finkbeiner & Davis (1998) with the additional latitude-dependent correction of Kunder et al. (2017). Finally, we have removed stars which are likely members of the Sagittarius stream by rejecting stars that satisfy the following three
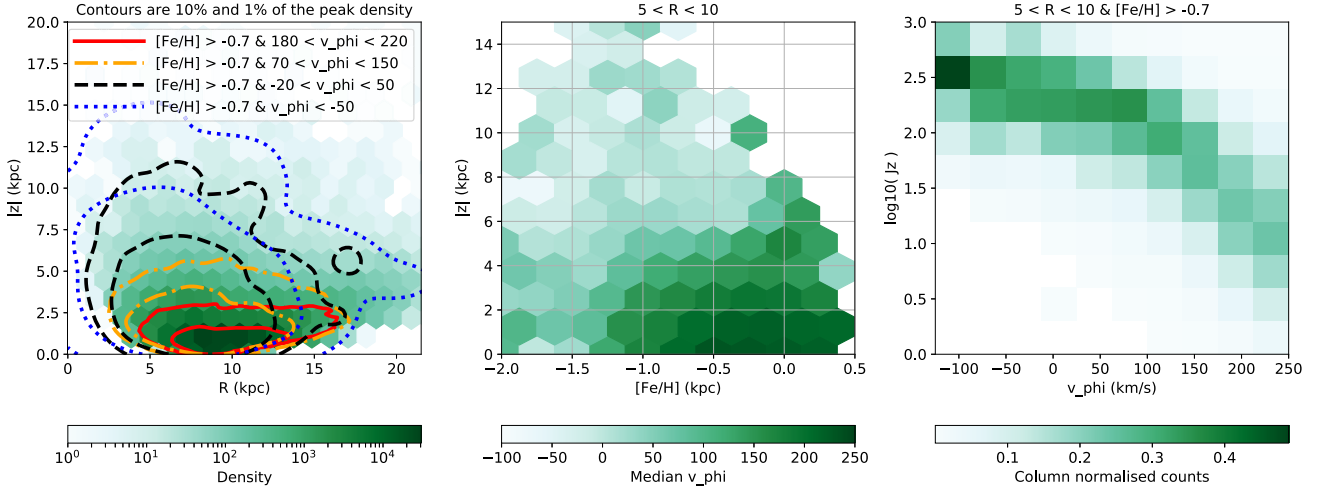
Figure 8. Using LAMOST K-giants to probe the spatial extent of the Splash. The left-hand panel shows the distribution of metal-rich stars of various v_ϕ. The middle panel shows the variation of v_ϕ with $|z|$ and [Fe/H], illustrating how at the intermediate metallicity ($-1 <$ [Fe/H] < -0.3) population transitions from being dominated by the higher angular momentum thick disc at $|z| \lesssim 5$ kpc to being dominated by the lower angular momentum Splash at $|z| \gtrsim 5$ kpc. The right-hand panel shows that for the higher angular momentum stars, there is a strong correlation between v_ϕ and J_z, but for the Splash stars ($v_\phi \lesssim 50$ km s^{-1}) this trend appears to flatten.

criteria: within 20 deg of the stream centre according to Belokurov et al. (2014); within 20 km s^{-1} of the stream radial velocity at that location according to Belokurov et al. (2014); and distance within 40 per cent of the distance at that location according to Hernitschek et al. (2017). Our resulting sample consists of 2 56 000 stars to distances up to 20 kpc. If we focus on metal-rich stars with [Fe/H] > -0.7 dex, we have 6106 with $|z| > 3$ kpc and 779 with $|z| > 5$ kpc.

The properties of these LAMOST K-giants are illustrated in Fig. 8. The left-hand panel shows the spatial distribution of all stars (grey scale), together with various subsets of metal-rich stars. The higher angular momentum populations, with [Fe/H] > -0.7 and $70 < v_\phi < 220$ km s^{-1} are clearly confined to the plane, with $|z| \lesssim 5$ kpc. As has been shown for the SDSS K-giants, the Splash stars reach much higher, to around 10 kpc. Note that since we are restricting ourselves to a specific range of [Fe/H] we are minimizing the influence of any metallicity-dependent bias in the distances. The middle panel shows that there is a transition in v_ϕ at $|z| \sim 5$ kpc, with the higher angular momentum stars confined to smaller $|z|$. The right-hand panel shows how the vertical extent, as quantified by the vertical action J_z, depends on v_ϕ. Actions have been calculated using the GALPY package (Bovy 2015), adopting the MWPotential2014 model for the potential. For the higher angular momentum stars (i.e. the 'canonical' thick disc with $v_\phi \gtrsim 100$ km s^{-1}) there is a strong correlation between v_ϕ and J_z, but for the Splash stars ($v_\phi \lesssim 50$ km s^{-1}) this trend appears to flatten.
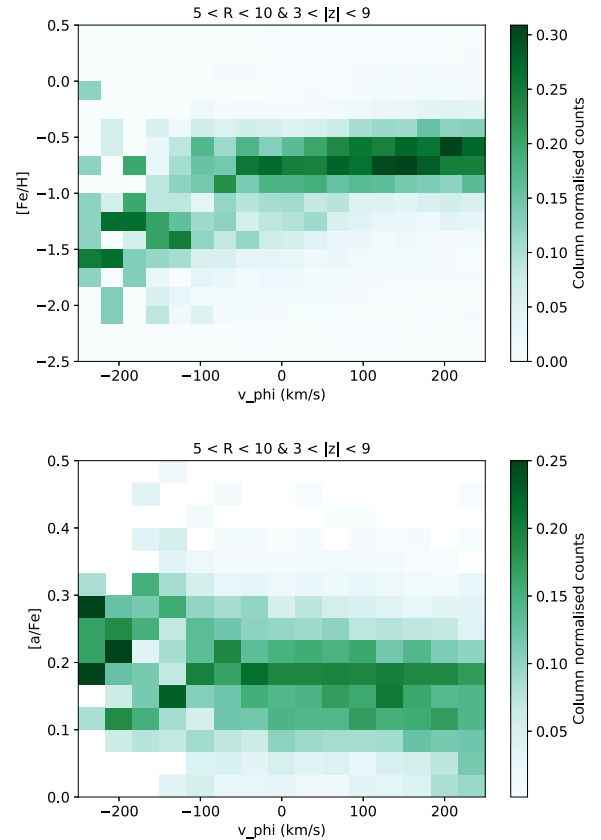
In Fig. 9, we illustrate the chemical properties of the Splash for the LAMOST K-giants, concentrating on the interface between the thick disc and the Splash ($3 < |z| < 9$ kpc). The upper panel shows how the intermediate-metallicity stars, which would normally be associated to the thick disc, stretch to very low angular momenta and even extend to negative v_ϕ. In terms of [Fe/H] these stars appear to be a homogeneous population. A similar conclusion can be drawn from the alpha-element abundance of these stars, which again appears homogeneous over a wide span of v_ϕ. Until one reaches the halo material at $v_\phi \lesssim -50$ km s^{-1}, most of the stars are concentrated at [α/Fe] $\sim +0.2$, which is what one expects for the thick disc population.

Figure 9. The chemical properties of the Splash for the LAMOST K-giants, concentrating on the interface between the thick disc and the Splash ($3 < |z| < 9$ kpc). The upper panel shows how the intermediate-metallicity stars, which appear to be a chemically homogeneous population, extend to negative v_ϕ. The lower panel, which shows the alpha-element abundance of these stars, again demonstrates the chemically homogeneous nature of stars over a wide span of v_ϕ.

5 DISCUSSION AND CONCLUSIONS

5.1 Making a Splash

Here, we tease out the details of the Splash formation from the existing cosmological simulations of MW-like galaxies.

5.1.1 Auriga simulations

The Auriga project (Grand et al. 2017) is one of the largest suites of magnetohydrodynamical high-resolution Galaxy simulations currently available. Auriga uses the 'zoom-in' technique (Frenk et al. 1996; Jenkins 2013) and the tree-PM moving-mesh code AREPO (see Springel 2010). The subgrid physics model comprises a spatially uniform photoionizing UV background, primordial and metal line cooling, SF, stellar evolution and supernovae feedback, supermassive black hole growth and feedback, and magnetic fields. A fixed set of chemical elements, including Fe and H, have been consistently tracked within the simulations. Haloes and bound (sub-)structures were identified using the FOF and SUBFIND algorithms (see Davis et al. 1985; Springel, Yoshida & White 2001). MW analogues were selected from the 100^3 Mpc^3 Dark Matter-only periodic box of the EAGLE project (Crain et al. 2015; Schaye et al. 2015), based on their virial mass, $\sim 10^{12}$ M$_\odot$, and an isolation criterion. The cosmological parameters adopted for the simulations are those of Planck Collaboration XVI (Planck Collaboration et al. 2014). In practice, we use the publicly available Aurigaia mock catalogues described in Grand et al. (2018b), which provide access to the present-day properties of the stellar particles for six of the Auriga haloes which have been simulated at the highest resolution level, (L3) with a baryonic mass resolution of $\sim 10^4$ M$_\odot$. These six haloes (nos 6, 16, 23, 24, and 27) are a subset of the original 30 haloes published in Grand et al. (2017). We use the no-extinction, ICC branch of the Aurigaia with the fiducial 30° angle for the Solar position. The ICC Aurigaia data sets are produced with the method of Lowing et al. (2015) to generate mock stars from simulation star particles. In our analysis, we include stars bound to the MW analogues (not to the satellites) and decrease the metallicity ([Fe/H]) of stars by a constant value of 0.5 dex in accordance with Fattahi et al. (2019).

Fig. 10 shows the behaviour of the azimuthal velocity as a function of metallicity (first and second columns) and age (third and fourth columns) for stellar particles in Auriga 6, 23, and 27. Note that these galaxies are amongst the ones with a highly radial stellar halo component as shown in Fattahi et al. (2019). Moreover, Auriga 23 is the clearest example of the [α/Fe] bimodality as described in Grand et al. (2018a). We also checked the other three Aurigaia mocks and found the behaviour consistent with what is presented below. To make comparison with the data (as discussed in Section 2) more appropriate, we limit the stellar particles to those with $5 < R$/kpc < 11 and $0.5 < |z|$/kpc < 3. The left-hand column of the figure shows the row-normalized density of stars in the plane of v_ϕ and [Fe/H] and can be compared directly with the observed distribution shown in the third panel of Fig. 1. Each of the three Auriga galaxies considered display a feature similar to the thin–thick disc chevron at high [Fe/H] as well as the low angular momentum overdensity at lower [Fe/H]. The next (second) column gives the distribution of the median age in the plane of v_ϕ and [Fe/H]. As noted earlier, the upper portion of the chevron is composed of the thin disc stars, which is confirmed by the purple and dark blue colours (i.e. typical ages <6 Gyr) in the region of the diagram. Moving along the lower portion of the chevron, one encounters a strong age gradient, supporting the inside-out thick

disc growth hypothesis discussed in Schönrich & Mcmillan (2017). The metal-rich Splash stars with low angular momentum can also be seen in the second panel in the case of Auriga 23 and 27 where the last major merger happened some 10 Gyr ago. In these two cases, at [Fe/H] > -1, the colour changes from blue to green to yellow and orange on moving from high positive v_ϕ to low and negative values. In Auriga 6, the last significant merger happened later, ∼8 Gyr ago, thus the Splash has the median age of the thick disc and the corresponding green colour. Please note that in the discussion above, instead of oversimplified 'the last major merger', a more appropriate nomenclature perhaps would be 'the last major that reached the Solar neighbourhood'. Interestingly, the end phases of the mergers as measured here match well those reported in Fattahi et al. (2019): the differences are typically within 0.3 Gyr.

The third column of Fig. 10 is the analogue of the left-hand panel in Fig. 4 and shows the dependence of v_ϕ on stellar age for the metal-rich stars in the three Auriga galaxies. The vertical Splash column is clearly visible in all cases considered here. Vertical red line gives an approximate young edge of the Splash and is calculated as the 20th percentile of the age distribution of the metal-rich stars with $v_\phi < 0$. Note that in all examples, the 'thick' (slow) disc population continues to form after the major merger. In the fourth column, we split the v_ϕ–age distribution into accreted (blue) and *in situ* (red) components. Note that the edge of Splash (shown with the vertical red line, see the previous panel) coincides perfectly with the end of the major accretion event in all three cases. We conjecture that (i) the youngest of the (local) retrograde *in situ* and accreted stars correspond to the final stages of a major merger event which (ii) heats up the pre-existing *in situ* population kicking it on to highly eccentric orbits.

In what follows we attempt to use the information in hand to deduce the pre-Splash conditions indirectly (a more in-depth analysis of the early state of the Auriga galaxies will be presented in Grand et al. (2020). Accordingly, the horizontal red line marks the median v_ϕ of the Splash stars, i.e. those to the left of the vertical red line. In the case of Auriga 6 and 23 where the median azimuthal velocity of the Splash stars is $100 < v_\phi < 200$, it is clear that the galaxy was in a protodisc state before the accretion as it managed to retain much of its angular momentum. The case of Auriga 27 is less clear; this galaxy could have started in a spheroid configuration which was further heated by the massive accretion event. Finally, the fifth column of Fig. 10 presents the age distributions for the accreted (blue), *in situ* (red), and Splash (black) stars (compare to the middle panel of Fig. 4). In all cases, the accreted population is typically older than that of the Splash in agreement with the observations presented above. In terms of the local SF activity, the SF rate typically increases significantly during the merger (continuous rise in the number of stars formed) and subsides immediately after (as indicated by a reasonably flat distribution of ages to the right of the vertical red line).

Fig. 11 displays the present-day density distributions of the accreted (blue), and *in situ* (red and black) populations in Auriga 6 (left), 23 (middle), and 27 (right). To gain an uninterrupted view of the Galaxy using the Aurigaia mock catalogues, we limit the stellar tracers to those with absolute magnitude $M_V < -2$. In this figure, we split the *in situ* population into two categories: the Splash (red contours), i.e. stars born at least 0.5 Gyr before the end of the major merger as indicated by the vertical red line in Fig. 10 and those born after (black contours). Structurally, Splash appears to be a smaller version of the accreted halo, somewhat reminiscent of a fluffy classical bulge. It is much rounder in shape compared to the rest of the *in situ* stars, that are mostly found at the low Galactic
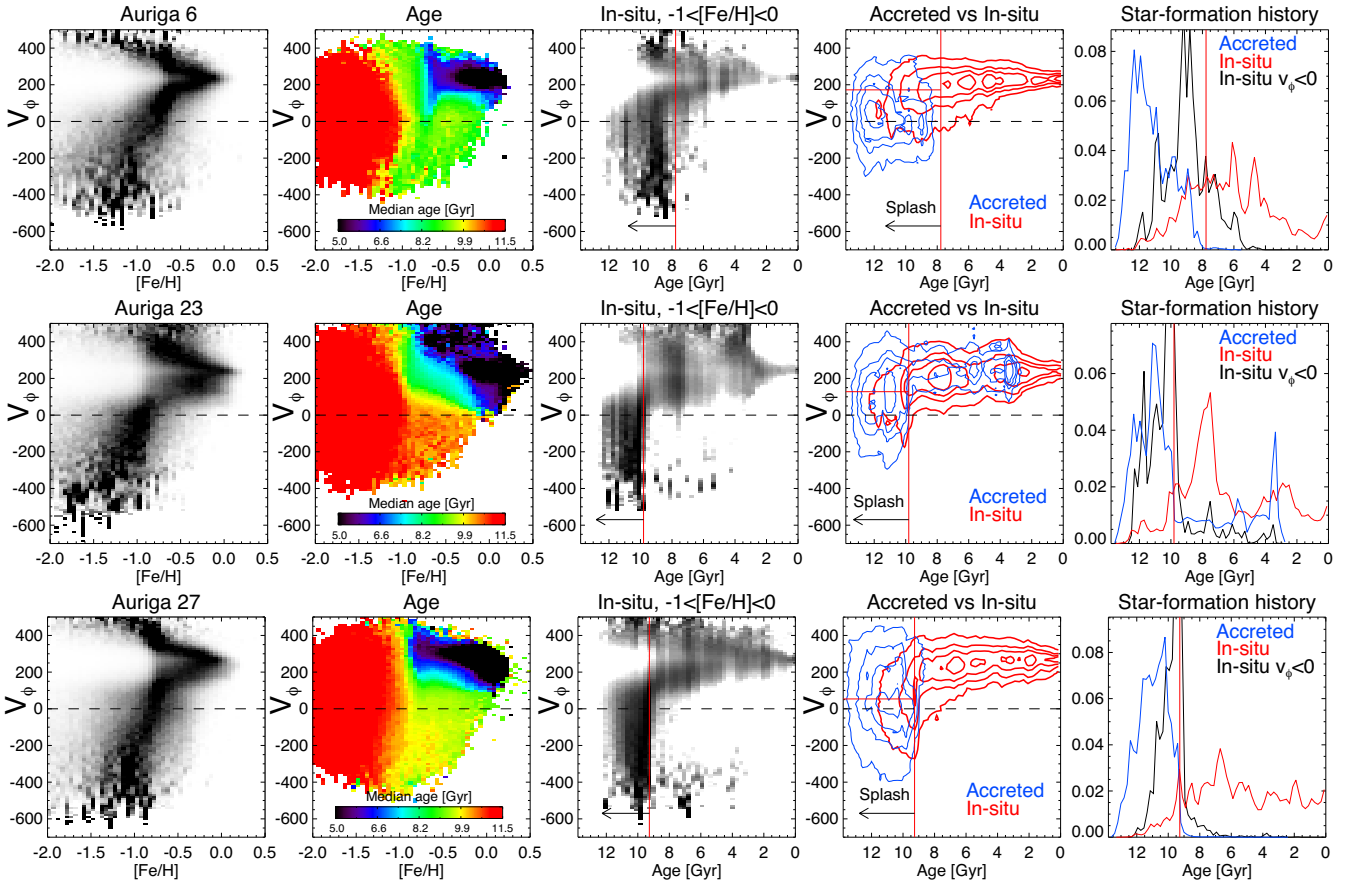
Figure 10. Solar neighbourhood in Auriga 6 (top), 23 (middle), and 27 (bottom). Only stars with $5 < R < 11$ and $0.5 < |z| < 3$ are included. First column is the numerical counterpart of top third panel of Fig. 1 and shows row-normalized density in the space of v_ϕ and metallicity. Note the thin–thick disc chevron feature at high [Fe/H] and the low angular momentum overdensity at lower [Fe/H]. Second column gives the median age distribution in the same space (compare to the bottom right panel of Fig. 1). The top (thin disc) part of the chevron is predominantly young age. In Auriga 23 and 27, where the last major merger happened some 10 Gyr ago, a clear Splash-like feature is visible for stars with [Fe/H] > -1 and $v_\phi < 0$. Third column is the analogue of the left-hand panel in Fig. 4 and shows the dependence of v_ϕ on stellar age for all metal-rich stars. The vertical Splash column is clearly visible in all three Auriga galaxies considered here. Vertical red line gives an approximate young edge of the Splash, signifying the end of the major merger. This value is calculated as the 20th percentile of the age distribution of the metal-rich stars with $v_\phi < 0$. Note that in all examples, the 'thick' (slow) disc population continues to form after the major merger. Fourth column the v_ϕ–age distribution is split into accreted (blue) and *in situ* (red) components. Note that the edge of Splash (shown with the vertical red line, see the previous panel) coincides perfectly with the end of the major accretion event. Horizontal red line gives the median v_ϕ of the Splash stars (i.e. those to the left of the vertical red line). In the case of Auriga 6 and 23, it is clear that the Galaxy was in a protodisc state before the accretion as it managed to retain much of the angular momentum. The case of Auriga 27 is less clear, it could have started in spheroid (rather than a disc) configuration. Finally, fifth column presents the age distributions for the accreted (blue), *in situ* (red), and Splash (black) stars (compare to the middle panel of Fig. 4). In all cases, the accreted population is typically older than that of the Splash. In terms of the local SF activity, the SF rate typically increases during the merger and subsides immediately after.

heights. In all three Auriga examples, the Splash does not extend much beyond 10–15 kpc in both R and z dimensions.

5.1.2 Latte simulations

The Latte project (Wetzel et al. 2016) is a suite of ∼10 hydrodynamical simulations of MW mass galaxies. As with Auriga, the simulations use a zoom-in technique, selecting MW analogues, based on their virial mass ($1 - 2 \times 10^{12}\,M_\odot$) and an isolation criterion, from a dark-matter-only periodic box of 85.5^3 Mpc^3 in a ΛCDM cosmology. The simulations utilize the GIZMO code (Hopkins 2015) which implements a mesh-free finite-mass method to solve the hydrodynamics and the tree-PM solver from GADGET-3 (Springel 2005) for the gravity. The subgrid physics model, FIRE-2 (Feedback In Realistic Environments, Hopkins et al. 2018), implements radiative heating and cooling including metal-line

cooling tracking 11 elements, a spatially uniform UV background and a set of stellar feedback processes.

The *ananke* project (Sanderson et al. 2018) used three of the Latte simulations (m12f, m12i, and m12m) to generate mock *Gaia* observations of MW-like simulations. This employed the resampling technique from Sharma et al. (2011) coupled with a set of stellar isochrones (Bressan et al. 2012). The dust extinction is generated self-consistently from the gas in the simulation assuming dust traces metal-rich gas. For each simulation, three different solar locations are employed. We have extracted a solar neighbourhood sample of 100 000 stars from the *ananke* mock Gaia catalogue for the m12f simulation (using the Sun location lsr0) subject to the selection: parallax> 0.5 mas, $|b| > 15$ deg, and $G < 17$, which approximately resembles the selection from a typical spectroscopic survey. Of the three simulations, m12f (first presented in Garrison-Kimmel et al. 2017) was selected due to its resemblance to the
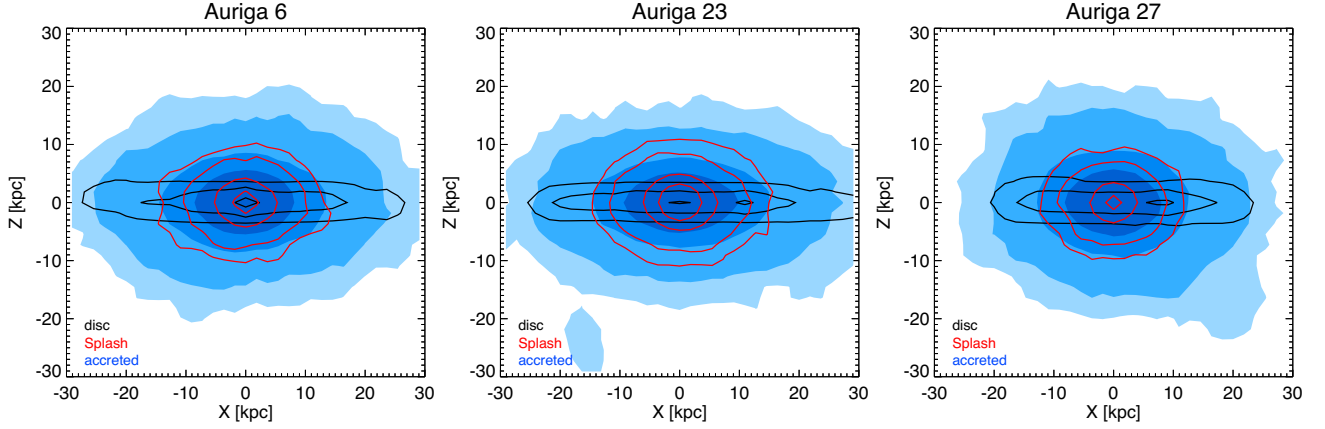
Figure 11. Present-day density distribution in Auriga 6 (left), 23 (middle), and 27 (right). Accreted (blue filled-in contours), *in situ* after Splash (black) and Splash (red) populations are shown. The Splash stars are selected to have the age at least 0.5 older than that marked by the vertical red line in Fig. 10 and v_ϕ < 100 km s^{-1}. Contours for both the accreted halo and the Splash populations are at the same density levels corresponding to the 50th, 70th, 90th, and 96th percentiles of the star count values. The disc contours are at the 92nd, 97th, and 99.8th percentiles of the disc density values.

MW. For example, the stars exhibit a bimodal [α/Fe]–[Fe/H] distribution.

In Fig. 12, we show the distributions of our selected sample in the spaces of age versus metallicity and age versus azimuthal velocity. We observe that the MW chemical evolution proceeds as expected up to a metallicity of ~ -0.3 dex at 6.5 Gyr. At this point a merger event (shown clearly by the hotter σ_R and σ_z kinematics and lower chemical evolution track) occurs (there is an additional smaller merger event at ~ 10.5 Gyr). This merger epoch corresponds to the youngest ages for counter-rotating metal-rich ([Fe/H] > -0.4) stars, coincides with a slight resetting of the metallicity track (upper left panel) as metal-poor accreted gas dilutes the MW gas and signifies the point at which the radial dispersion suddenly drops (third lower panel but see also see fig. 3 of Sanderson et al. 2018). It is this feature of m12f that gives rise to the bimodal [α/Fe]–[Fe/H] distribution. After this merger epoch, SF accelerates (note the rise in the black density contours), likely prompted by the merger event, and disc evolution proceeds in a more regular fashion with essentially no counter-rotating stars. The chevron structure of the thin and thick discs is visible after the merger demonstrating that thick disc-like evolution can occur *after* the merger event (even for stars formed long after the merger, a bimodal chemical distribution persists). Quantitatively, the dispersions of the different populations correspond nicely to the figures in Table 1. The young thin disc stars (defined as [Fe/H] > -0.4, age < 1.5 Gyr, and v_ϕ > 200 km s^{-1} – corresponding almost exclusively to the low-alpha sequence) have dispersions in R and z of (61, 30) km s^{-1} respectively. The thick disc (defined as [Fe/H] > -0.4, 4.5 < age / Gyr < 6.5 and 100 < v_ϕ < 200 km s^{-1} – corresponding to the high alpha sequence) has (93,66). The Sausage-like merger remnant (defined as [Fe/H] < -0.4, 6.5 < age / Gyr < 9.5 and v_ϕ < 0) has (219, 129) and finally the Splash-like MW component (defined as [Fe/H] > -0.4, age >6.5 Gyr, and v_ϕ < 0) has (153, 101). In general, the simulation is kinematically hotter than the MW (Sanderson et al. 2018), but the hierarchy and respective ratios show good correspondence with the observations. Finally, we present the density distributions of the different components in Fig. 13. The distribution is very similar to that observed in the analogous Auriga plots in Fig. 11. Here, we define the components in a similar way as for the local sample but requiring the disc has age< 6 Gyr and v_ϕ > 150 km s^{-1}, and using a by-eye chemical evolution track in age–metallicity space

to separate out the *in situ* from accreted halo. We observe that the Splash component is spheroidal with a similar flattening to the accreted component. Without full histories of the star particles we cannot state definitively that the simulation reflects the Splash hypothesis presented in this paper. However, it seems highly likely. An alternative, more unlikely hypothesis is that the protodisc was near spheroidal and after the merger a much colder gas disc formed.

5.2 Virial considerations

Finally, we can cross-check our ideas by using the virial theorem to estimate the mass M_s of the infalling satellite. As the satellite falls a distance Δr, then it loses energy

$$\Delta E \approx -M_s \frac{\mathrm{d}\phi}{\mathrm{d}r} \Delta r \approx -\frac{M_s v_0^2}{r} \Delta r, \tag{1}$$

where ϕ is the total potential, and the Galaxy is assumed to have a flat rotation curve v_0. The energy loss of the satellite under dynamical friction is pumped into heating both the protodisc and the halo. As the Sausage encounter is low inclination, we assume that most of the heating takes place in the protodisc to produce both the thick disc and the Splash.

Some of the energy deposited in the protodisc is converted to potential energy, as the disc thickens in response to the vertical heating. We use the virial theorem (per unit surface area of the disc) to estimate how ΔE turns into kinetic and potential energy. The vertical component reads

$$2T + W \approx 0, \tag{2}$$

where we have discarded the time-dependent term as we are assuming the system settles into equilibrium after the encounter has ended. If H is the scale height of the protodisc and Σ the surface density, then the kinetic and potential energy (per unit surface area) are

$$T \approx \frac{1}{2} \Sigma \sigma_z^2, \qquad W_1 \approx -\pi G \Sigma^2 H. \tag{3}$$

The protodisc has a total potential energy $W = W_1 + W_2$ because it resides in the gravitational potential of itself and the dark halo, with the latter term for a flat rotation curve galaxy being

$$W_2 \approx -\frac{3}{2} \Sigma H^2 G \frac{M_h(r)}{r^3}. \tag{4}$$
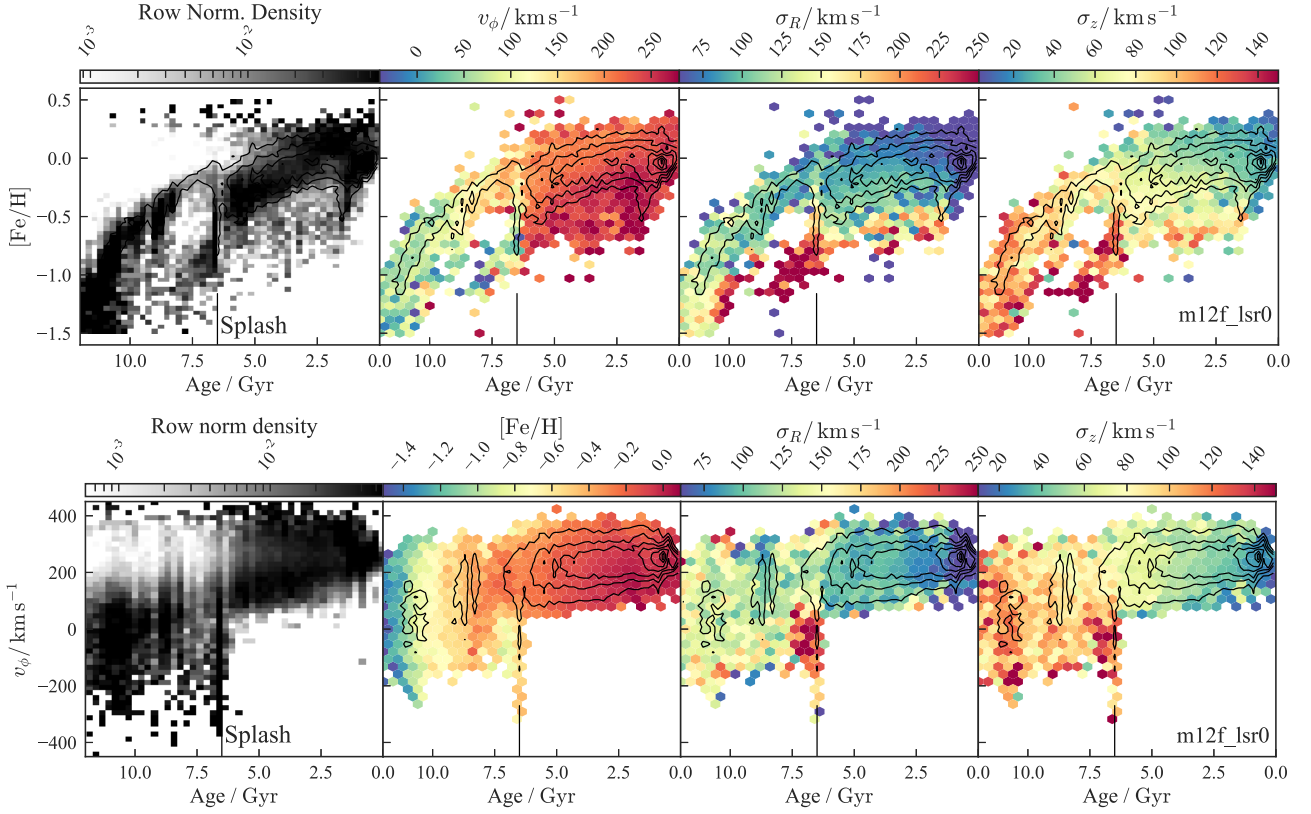
Figure 12. Solar neighbourhood stars selected from the *ananke Gaia* mock for the Latte simulation m12f. The stars were selected to have parallaxes > 0.5 mas, $|b| > 15$ deg, and $G < 17$. The top row of panels shows the row normalized density, mean azimuthal velocity, radial dispersion, and vertical dispersion in bins of age versus metallicity. The bottom row shows similar in the plane of age versus azimuthal velocity. Note the Sausage-like merger event (marked with the vertical line) corresponding to the youngest metal-rich counter-rotating Splash stars, a subsequent increase in SF and an increase in the radial velocity dispersion for stars older than the event. The contours are equally spaced in square root of the number density.

The total energy change $\Delta E = \Delta T + \Delta W$, and so using the virial theorem

$$\frac{1}{2} \times \frac{\Delta E}{2\pi r \Delta r} \approx \frac{\pi}{2} G\Sigma^2 \Delta H \left(1 + 3\frac{HM_h(r)}{\pi r^3 \Sigma} \right), \quad (5)$$

where we have assumed that only half the energy change goes into vertical heating (and the other half into radial heating). Inserting equation (1), we obtain for the change in scale height of the protodisc

$$\Delta H \approx \frac{M_s v_0^2}{2\pi^2 G\Sigma^2 r^2}, \quad (6)$$

where we have omitted the small correction term in brackets in equation (5), which is of the order 15 per cent. This gives the change in vertical velocity dispersion of the protodisc as

$$\Delta \sigma_z^2 \approx \frac{M_s v_0^2}{2\pi\Sigma r^2}. \quad (7)$$

We now assume that the protodisc density law Σ is of Mestel form and that it provides half the contribution to v_0 locally, with the dark halo providing the rest. Normalizing to the Solar neighbourhood, we obtain

$$\Delta \sigma_z^2 \approx 0.25 v_0^2 \left(\frac{M_s}{M_{disc}} \right) \left(\frac{R_\odot}{r} \right). \quad (8)$$

where M_{disc} is the mass contained within $R_\odot$. Referring to the velocity dispersions in Table 1, we now assume that the encounter excited both the stars now in the Splash and the thick disc. This

gives $\Delta\sigma_z^2 \approx 2700$ km^{2}s^{-2} (using the data in Table 1 and weighting the thick disc and the Splash by their fractional contribution).

Assuming that the amplitude of the flat rotation curve is $v_0 = 230$ km s^{-1}, this finally gives

$$\left(\frac{M_s}{M_{disc}} \right) \approx 0.20. \quad (9)$$

On energetic grounds, the Sausage is able to excite stars vertically into thick disc and Splash orbits if it is roughly an order of magnitude less massive than the protodisc.

5.3 What's in the Splash?

As shown clearly from Fig. 4, the bulk of the MW stars with ages similar to that of the Splash carry plenty of angular momentum today, implying that before the massive ancient merger the Galaxy was likely a protodisc. The most direct interpretation of this observation (also supported by our analysis of the hydrodynamical zoom-in simulations discussed above; see Figs 10 and 12) is that the Splash is composed of the stars dispersed from the protodisc of the Galaxy during the accretion event which created the GS. In this regard, of the many scenarios of *in situ* halo formation proposed in the literature, the heated *in situ* channel – as discussed in McCarthy et al. (2012) – appears to be the most viable, at least here, in the MW. In this picture, the Splash may simply represent the most energetic portion of the thick disc. The seemingly smooth transition from the
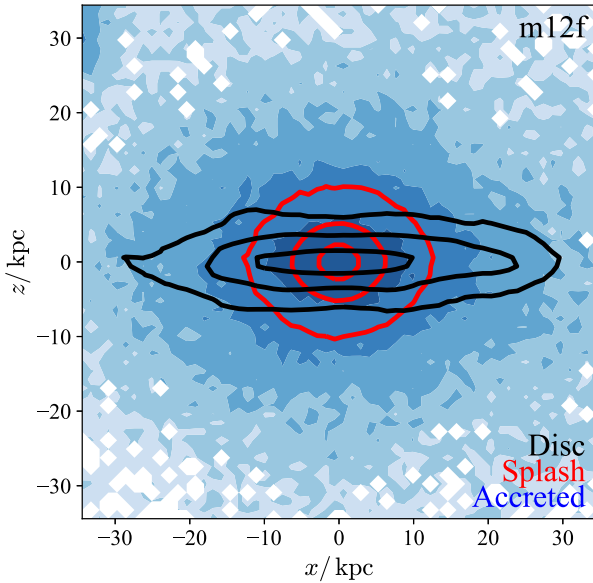
Figure 13. Present-day density distribution for Latte simulation m12f (analogous to Fig. 11 for the Auriga simulations). The disc component is metal-rich ([Fe/H] > −0.4), rotating (v_ϕ > 150 km s^{-1}) and young (age<6 Gyr). The Splash and accreted components are old (age>7 Gyr), retrograde (v_ϕ < 0) and split by tracks in age–metallicity space. We employ a further cut at age = 9.5 Gyr to define the accreted component so as to avoid contamination from *in situ* stars. Contour levels are drawn at 0.1, 1, and 10 per cent of the peak density for the Splash and the disc, and additionally at 0.315, 3.15, and 31.5 for the accreted component.

Splash to the thick disc as observed in the many panels of Fig. 1 would argue in favour of this interpretation. On the other hand, the Splash appears to be an additional component in the (albeit rather simplified) azimuthal velocity decomposition presented in Fig. 2. Another important difference between the two components is that, according to Figs 4, 10, and 12, the Splash formed only during the last major merger, while the thick disc appears to have formed before, during and after the event. For example, the left-hand panel of Fig. 4 shows that the thick disc formation likely continued until 8 Gyr ago, i.e. 1–2 Gyr after the Splash, in good agreement with previous studies (see e.g. Haywood et al. 2013).

Note however that given the data in hand, it is impossible to completely rule out other (perhaps more exotic) modes of the Splash's formation. Apart from the possibilities already discussed in Cooper et al. (2015), let us point out two additional channels: first, given the relatively early time of the GS merger, it is quite likely that in the accretion event, in addition to the dark matter and stars, large amounts of unused gas were also dumped on to the nascent MW. In such a gas-rich merger, the violent interaction between the gaseous discs of the two galaxies could toss the gas clouds around, causing some of the promoted SF to occur on rather eccentric, halo-like orbits. Another Splash formation mechanism can operate within gaseous outflows launched as a result of the profuse galactic feedback, induced either by SF or active galactic nucleus activity. Maiolino et al. (2017) present the first unambiguous example of ongoing SF within a galactic outflow. Subsequently, Gallagher et al. (2019) demonstrate that at least ∼ 30 per cent of all outflows in the MaNGA DR2 samples exhibit clear signs of SF, in agreement with the independent analysis of the MaNGA (Mapping Nearby Galaxies at Apache Point) data by Rodríguez del Pino et al. (2019). These striking discoveries have been preceded

by a decade of mounting evidence for molecular gas outflows (see e.g. Feruglio et al. 2010; Sturm et al. 2011; Cicone et al. 2014). Furthermore, a number of independent analytical and numerical models now exist that substantiate the possibility of SF on highly radial orbits within galactic outflows (e.g. Ishibashi & Fabian 2012; Zubovas et al. 2013; Ishibashi, Fabian & Canning 2013; Zubovas & King 2014; Wang & Loeb 2018; Decataldo et al. 2019). These findings imply that SF activity within outflows is ubiquitous; as noted by Gallagher et al. (2019), regular isolated disc galaxies bear signs of this process. As is clear from the right-hand column of Fig. 10, the SF rate increases sharply during the last major merger, thus creating conditions favourable for the production of the Splash population inside the feedback-induced outflowing gas. Maiolino et al. (2017) and Gallagher et al. (2019) discuss the fate of the stars born this way. They note that it is currently impossible to have a meaningful constraint on the orbital properties of the outflow-born stars. However, they conjecture that as soon as the stars are born, they decouple from the outflow and continue their motion in the host's potential ballistically. They estimate that the bulk of this population will be limited to the inner few kpc of the Galaxy in good agreement with our measurements of the extent of the Splash. We envisage that future studies of the chemical abundance gradients across the Splash may shed light on the genesis of this population.

5.4 Conclusions

We have analysed orbits, ages and alpha abundances of a large sample of nearby stars, focusing on the metal-rich, −0.7 < [Fe/H] < −0.2 population of stars with low angular momentum, which we name the Splash. Our principal findings are summarized below.

(i) In terms of metallicity, the Splash can be seen most easily between [Fe/H] = −0.7 and −0.2 (as already seen in Bonaca et al. 2017; Haywood et al. 2018; Di Matteo et al. 2018; Gallart et al. 2019). More metal-poor stars typically have more eccentric orbits and larger vertical velocity dispersion, while more metal-rich stars have higher angular momentum (see middle row of Fig. 1). Note however that we do not imply that the Splash population is limited to this range of iron abundance and believe that it likely stretches to lower values of [Fe/H], where it is overwhelmed by the accreted stars. Recently, Sestito et al. (2019) detected a significant number of ultra metal-poor stars with orbits confined to the disc plane. These stars could well be the denizens of the Galaxy's protodisc which was heated by massive accretion events (in line with the conclusions reached in their paper). Their result also implies that there exists a population of ancient stars whose orbits have not been much affected by the cataclysmic events that lead to the creation of the GS. This can be explained if not all of the protodisc was destroyed. In that case however, it is difficult to imagine how stars at large distances from the Galactic centre could remain unaffected. Perhaps instead, these stars were born in a disc-like configuration during or immediately after the last major merger. Alternatively, it is easier to preserve the Galactic protodisc, if the Splash was created via a process that does not require the disc destruction (see e.g. Section 5.3). Finally, these stars may have been 'protected' in the inner Galaxy during the merger event, and then migrated outwards. This scenario requires efficient radial migration in the (potentially narrow) window between the merger event and the Galactic bar forming and subsequently trapping stars in the inner Galaxy.

(ii) We show that in the v_ϕ–[Fe/H] plane there exists a chevron-like feature, resembling a > sign and corresponding to the 'thin–thick' disc bifurcation. The Splash is located at and below the break

in the v_ϕ–[Fe/H] sequence of the 'thick' disc and has metallicity typical of both the 'thick' and the 'thin' disc populations (third panel of the top row of Fig. 1). In fact, in many other dimensions studied here, the Splash connects smoothly to the 'thick' disc, e.g. azimuthal velocity, alpha abundances and ages. The Splash properties however are extreme compared to the bulk of the 'thick' disc. It has little angular momentum and plenty of retrograde stars, with most eccentricities in excess of $e > 0.5$, rather unusual for the disc. At a given metallicity, the Splash's alpha-abundances are typically the highest attained by the 'thick' disc stars (see bottom row of Fig. 1), while its ages are the oldest. We conclude (in agreement with Bonaca et al. 2017; Haywood et al. 2018; Di Matteo et al. 2018; Gallart et al. 2019) that the Splash is the ancient portion of the 'thick' or protodisc of the Galaxy.

(iii) The cleanest Splash selection is that delivered by two simple cuts: $v_\phi < 0$ and [Fe/H] > -0.7. This is the portion of the parameter space that suffers the lowest contamination and is where Amarante et al. (2019) detect Splash-like material (see their fig. 7). Note, however, that according to our kinematic modelling presented in Section 3, the Splash population reaches to much higher values of v_ϕ and has a clear net positive spin. Our three-component Gaussian model is rather naive, and should not be overinterpreted. However, it does show quite clearly both the necessity for an additional kinematic component (the knee at around $v_\phi \sim 0$ km s^{-1}) and the extent of this component to v_ϕ as high as 100–200 km s^{-1}. In connection to this, the recently discovered giant, prograde, and metal-rich stream Nyx (see Necib et al. 2019a) may well be nothing but a piece of the Splash. Additionally, it is interesting to point out that our high-metallicity boundary for the Splash population of < -0.2 (also see Di Matteo et al. 2018) coincides with the value of [Fe/H] where changes in the disc's chemodynamical properties had been noted before. For example, this is the highest metallicity where the bimodality in [α/Fe] can be established (see e.g. Nidever et al. 2014). This is also the boundary chosen by Snaith et al. (2015) to demarcate the inner and outer thin disc populations.

(iv) The Splash can be seen most clearly in Fig. 4 where it is visible as a vertical band of stars with a large range of v_ϕ limited to a constant and narrow range of ages (< 10 Gyr). We point out a strikingly synchronized truncation in the age distribution of the retrograde metal-poor (likely accreted) stars and the retrograde metal-rich (likely *in situ*) stars (see middle and right-hand panels of Fig. 4). In line with Gallart et al. (2019), we argue that the youngest age of the Splash stars can be used to date the last major merger experienced by the Galaxy, i.e the accretion that lead to the creation of the GS. Note, however, that we disagree with the conclusion of Gallart et al. (2019) that the SF histories of the halo and the Splash are indistinguishable. As the middle panel of our Fig. 4 clearly shows, the age distribution of the Splash stars peak some ~ 1 Gyr later. This is consistent with both (i) the fact that the Splash stars are significantly more metal-rich than those in the halo and (ii) the hypothesis that the Splash may originate from the protodisc, which would also require some time to assemble.

(v) We have also attempted to map the 3D structure of the Splash well beyond the Solar neighbourhood. We have obtained consistent constraints on the spatial extent and the shape of the Splash population using two independent data sets, that of Sanders & Das (2018) and the SDSS (Xue et al. 2014) and LAMOST K-giants. While near the Sun, there are as many metal-rich stars with $v_\phi < 100$ km s^{-1} as there are metal-poor ones, the ratio of metal-rich to metal-poor low-angular momentum stars drops quickly with Galactocentric radial distance and height. In particular, at $R > 15$ kpc and $|z| > 10$ kpc, this ratio can be ~ 5 per cent or lower

(see Figs 5, 6, and 8). The minuscule size of the Splash compared to the rest of the Galactic stellar halo or even the GS makes sense if the Splash was born out of the protodisc of the MW, itself believed to be rather small. Interestingly, the distribution of the oldest Galactic long-period variables also exhibits a sharp truncation around 15–20 kpc (see fig. 13 of Grady, Belokurov & Evans 2019). Fernández-Alvar et al. (2019b) use APOGEE spectroscopy and *Gaia* DR2 astrometry to identify three distinct groups of metal-rich [Fe/H] > -0.75 stars at Galactic heights of $|z| > 10$ kpc. They show that of these three, one can be associated with the Sgr stream (also see Section 4.2 of this paper) and one with the recently kicked-up disc stars in the anticentre region. The third and final group has a low-amplitude prograde rotation (decreasing with $|z|$) and high values of [Mg/Fe]. It is almost certain that this third group detected by Fernández-Alvar et al. (2019b) is part of the Splash.

(vi) We have inspected examples from the Auriga and Latte suites of cosmological zoom-in simulations of the MW's formation, finding that example galaxies in both suites produce a Splash-like structure as a result of the interaction of a massive dwarf galaxy with the pre-existing *in situ* (typically disc-like) population (in agreement with Bonaca et al. 2017; Monachesi et al. 2019). We show that the epoch of this major merger can be accurately calculated via two different routes: either relying on the youngest ages of the accreted stars observed locally at redshift $z = 0$ or using the ages of the metal-rich *in situ* stars on retrograde orbits. We find strong but indirect evidence that in several of the inspected Auriga simulations a protodisc is transformed into a more spheroidal Splash component by a massive merger event. All of the six Aurigaia galaxies analysed here have a detectable Splash population of varying significance, demonstrating how easy it is to kick up *in situ* stars on to halo-like orbits in agreement with Jean-Baptiste et al. (2017). We therefore propose to exploit the intimate connection between the last major merger and the Splash to calculate the mass of the in-falling satellite as well as the geometry and the kinematics of the merger (we describe a simple analytic attempt in Section 5.2). The details of the interaction between the GS progenitor and the *in situ* population as well as the ensuing transformation of the Galactic protodisc will be discussed in the upcoming publication (Grand et al. 2020).

The picture of the early days of the MW as painted by the observations and the simulations discussed here is complex. There is evidence that the influence of the last massive accretion event may well have been both destructive and constructive. The ancient head-on collision wrought havoc in the young Galaxy, heating, scrambling, and possibly truncating some of its disc. Yet it may have also helped to promote SF and delivered fresh gas supplies to be used in the subsequent disc growth. The MW never looked the same after the Biggest Splash.

REFERENCES

Abolfathi B. et al., 2018, ApJS, 235, 42
Amarante J. A. S., Smith M. C., Boeche C., 2019, MNRAS, 492, 3816
Belokurov V. et al., 2014, MNRAS, 437, 116
Belokurov V., Erkal D., Evans N. W., Koposov S. E., Deason A. J., 2018, MNRAS, 478, 611
Bird S. A., Xue X.-X., Liu C., Shen J., Flynn C., Yang C., 2019, AJ, 157, 104
Boeche C., Smith M. C., Grebel E. K., Zhong J., Hou J. L., Chen L., Stello D., 2018, AJ, 155, 181
Bonaca A., Conroy C., Wetzel A., Hopkins P. F., Kereš D., 2017, ApJ, 845, 101
Bovy J., 2015, ApJS, 216, 29
Bressan A., Marigo P., Girardi L., Salasnich B., Dal Cero C., Rubele S., Nanni A., 2012, MNRAS, 427, 127
Buder S. et al., 2018, MNRAS, 478, 4513
Bullock J. S., Johnston K. V., 2005, ApJ, 635, 931
Carollo D. et al., 2007, Nature, 450, 1020
Carollo D. et al., 2010, ApJ, 712, 692
Chen Y., Girardi L., Bressan A., Marigo P., Barbieri M., Kong X., 2014, MNRAS, 444, 2525
Chen Y., Bressan A., Girardi L., Marigo P., Kong X., Lanza A., 2015, MNRAS, 452, 1068
Cicone C. et al., 2014, A&A, 562, A21
Cooper A. P. et al., 2010, MNRAS, 406, 744
Cooper A. P., Parry O. H., Lowing B., Cole S., Frenk C., 2015, MNRAS, 454, 3185
Crain R. A. et al., 2015, MNRAS, 450, 1937
Cui X.-Q. et al., 2012, Res. Astron. Astrophys., 12, 1197
Das P., Sanders J. L., 2019, MNRAS, 484, 294
Davis M., Efstathiou G., Frenk C. S., White S. D. M., 1985, ApJ, 292, 371
De Lucia G., Helmi A., 2008, MNRAS, 391, 14
De Silva G. M. et al., 2015, MNRAS, 449, 2604
Deason A. J., Belokurov V., Evans N. W., 2011, MNRAS, 416, 2903
Deason A. J., Belokurov V., Evans N. W., Johnston K. V., 2013, ApJ, 763, 113
Deason A. J., Belokurov V., Koposov S. E., Gómez F. A., Grand R. J., Marinacci F., Pakmor R., 2017, MNRAS, 470, 1259
Deason A. J., Belokurov V., Koposov S. E., Lancaster L., 2018, ApJ, 862, L1
Deason A. J., Belokurov V., Sanders J. L., 2019, MNRAS, 490, 3426
Decataldo D., Pallottini A., Ferrara A., Vallini L., Gallerani S., 2019, MNRAS, 487, 3377
Di Matteo P., Haywood M., Lehnert M. D., Katz D., Khoperskov S., Snaith O. N., Gómez A., Robichon N., 2018, A&A, 632, A4
Fattahi A. et al., 2019, MNRAS, 484, 4471
Fernández-Alvar E. et al., 2019b, MNRAS, 487, 1462
Fernández-Alvar E., Tissera P. B., Carigi L., Schuster W. J., Beers T. C., Belokurov V. A., 2019a, MNRAS, 485, 1745
Feruglio C., Maiolino R., Piconcelli E., Menci N., Aussel H., Lamastra A., Fiore F., 2010, A&A, 518, L155
Font A. S., Johnston K. V., Bullock J. S., Robertson B. E., 2006, ApJ, 638, 585
Frenk C. S., Evrard A. E., White S. D. M., Summers F. J., 1996, ApJ, 472, 460
Gaia Collaboration et al., 2016, A&A, 595, A1
Gaia Collaboration et al., 2018a, A&A, 616, A1
Gaia Collaboration et al., 2018b, A&A, 616, A10
Gaia Collaboration et al., 2018c, A&A, 616, A12
Gallagher R., Maiolino R., Belfiore F., Drory N., Riffel R., Riffel R. A., 2019, MNRAS, 485, 3409
Gallart C., Bernard E. J., Brook C. B., Ruiz-Lara T., Cassisi S., Hill V., Monelli M., 2019, Nat. Astron., 3, 932
García Pérez A. E. et al., 2016, AJ, 151, 144
Garrison-Kimmel S. et al., 2017, MNRAS, 471, 1709
Gilmore G. et al., 2012, The Messenger, 147, 25
Grady J., Belokurov V., Evans N. W., 2019, MNRAS, 483, 3022
Grand R. J. J. et al., 2017, MNRAS, 467, 179
Grand R. J. J. et al., 2018a, MNRAS, 474, 3629
Grand R. J. J. et al., 2018b, MNRAS, 481, 1726
Grand R. J. J. et al., 2020, preprint (arXiv:2001.06009)
Haywood M., Di Matteo P., Lehnert M. D., Katz D., Gómez A., 2013, A&A, 560, A109
Haywood M., Di Matteo P., Lehnert M. D., Snaith O., Khoperskov S., Gómez A., 2018, ApJ, 863, 113
Helmi A., de Zeeuw P. T., 2000, MNRAS, 319, 657
Helmi A., White S. D. M., 1999, MNRAS, 307, 495
Helmi A., Babusiaux C., Koppelman H. H., Massari D., Veljanoski J., Brown A. G. A., 2018, Nature, 563, 85
Hernitschek N. et al., 2017, ApJ, 850, 96
Hopkins P. F. et al., 2018, MNRAS, 480, 800
Hopkins P. F., 2015, MNRAS, 450, 53
Iorio G., Belokurov V., 2019, MNRAS, 482, 3868
Ishibashi W., Fabian A. C., 2012, MNRAS, 427, 2998
Ishibashi W., Fabian A. C., Canning R. E. A., 2013, MNRAS, 431, 2350
Jean-Baptiste I., Di Matteo P., Haywood M., Gómez A., Montuori M., Combes F., Semelin B., 2017, A&A, 604, A106
Jenkins A., 2013, MNRAS, 434, 2094
Johnston K. V., Hernquist L., Bolte M., 1996, ApJ, 465, 278
Kawata D. et al., 2018, MNRAS, 473, 867
Koposov S. E. et al., 2011, ApJ, 736, 146
Kruijssen J. M. D., Pfeffer J. L., Reina-Campos M., Crain R. A., Bastian N., 2019, MNRAS, 486, 3180
Kunder A. et al., 2017, AJ, 153, 75
Lancaster L., Koposov S. E., Belokurov V., Evans N. W., Deason A. J., 2019, MNRAS, 486, 378
Lee Y. S. et al., 2011, ApJ, 738, 187
Lindegren L. et al., 2018, A&A, 616, A2
Lowing B., Wang W., Cooper A., Kennedy R., Helly J., Cole S., Frenk C., 2015, MNRAS, 446, 2274
Luo A.-L. et al., 2015, Res. Astron. Astrophys., 15, 1095
Mackereth J. T. et al., 2019, MNRAS, 482, 3426
Magnier E. A. et al., 2013, ApJS, 205, 20
Maiolino R. et al., 2017, Nature, 544, 202
Majewski S. R. et al., 2017, AJ, 154, 94
Martell S. L. et al., 2017, MNRAS, 465, 3203
Massari D., Koppelman H. H., Helmi A., 2019, A&A, 630, L4
Matsuno T., Aoki W., Suda T., 2019, ApJ, 874, L35

McCarthy I. G., Font A. S., Crain R. A., Deason A. J., Schaye J., Theuns T., 2012, MNRAS, 420, 2245

Meza A., Navarro J. F., Abadi M. G., Steinmetz M., 2005, MNRAS, 359, 93

Minchev I. et al., 2019, MNRAS, 487, 3946

Monachesi A. et al., 2019, MNRAS, 485, 2589

Myeong G. C., Evans N. W., Belokurov V., Sand ers J. L., Koposov S. E., 2018a, MNRAS, 478, 5449

Myeong G. C., Evans N. W., Belokurov V., Sand ers J. L., Koposov S. E., 2018b, ApJ, 856, L26

Myeong G. C., Evans N. W., Belokurov V., Sand ers J. L., Koposov S. E., 2018c, ApJ, 863, L28

Myeong G. C., Vasiliev E., Iorio G., Evans N. W., Belokurov V., 2019, MNRAS, 488, 1235

Necib L. et al., 2019a, preprint (arXiv:1907.07190)

Necib L., Lisanti M., Belokurov V., 2019b, ApJ, 874, 3

Nidever D. L. et al., 2014, ApJ, 796, 38

Nissen P. E., Schuster W. J., 2010, A&A, 511, L10

Nissen P. E., Schuster W. J., 2011, A&A, 530, A15

Piatti A. E., Carballo-Bello J. A., 2019, MNRAS, 485, 1029

Planck Collaboration et al., 2014, A&A, 571, A16

Robertson B., Bullock J. S., Font A. S., Johnston K. V., Hernquist L., 2005, ApJ, 632, 872

Rodríguez del Pino B., Arribas S., Piqueras López J., Villar-Martín M., Colina L., 2019, MNRAS, 486, 344

Sanders J. L., Das P., 2018, MNRAS, 481, 4093

Sanderson R. E. et al., 2018, ApJS, 246, 6

Schaye J. et al., 2015, MNRAS, 446, 521

Schlegel D. J., Finkbeiner D. P., Davis M., 1998, ApJ, 500, 525

Schönrich R., Aumer M., 2017, MNRAS, 472, 3979

Schönrich R., Mcmillan P. J., 2017, MNRAS, 467, 1154

Schönrich R., Asplund M., Casagrande L., 2011, MNRAS, 415, 3807

Schönrich R., Binney J., Asplund M., 2012, MNRAS, 420, 1281

Schönrich R., McMillan P., Eyer L., 2019, MNRAS, 487, 3568

Schuster W. J., Moreno E., Nissen P. E., Pichardo B., 2012, A&A, 538, A21

Sesar B., Jurić M., Ivezić, Ž., 2011, ApJ, 731, 4

Sestito F. et al., 2019, MNRAS, 484, 2166

Sharma S., Bland-Hawthorn J., Johnston K. V., Binney J., 2011, ApJ, 730, 3

Simion I. T., Belokurov V., Koposov S. E., 2019, MNRAS, 482, 921

Skrutskie M. F. et al., 2006, AJ, 131, 1163

Snaith O., Haywood M., Di Matteo P., Lehnert M. D., Combes F., Katz D., Gómez A., 2015, A&A, 578, A87

Springel V., 2005, MNRAS, 364, 1105

Springel V., 2010, MNRAS, 401, 791

Springel V., Yoshida N., White S. D. M., 2001, New Astron., 6, 79

Steinmetz M. et al., 2006, AJ, 132, 1645

Sturm E. et al., 2011, ApJ, 733, L16

Tang J., Bressan A., Rosenfield P., Slemer A., Marigo P., Girardi L., Bianchi L., 2014, MNRAS, 445, 4287

Tian H., Liu C., Xu Y., Xue X., 2019, ApJ, 871, 184

Tissera P. B., White S. D. M., Scannapieco C., 2012, MNRAS, 420, 255

Vincenzo F., Spitoni E., Calura F., Matteucci F., Silva Aguirre V., Miglio A., Cescutti G., 2019, MNRAS, 487, L47

Wang X., Loeb A., 2018, New Astron., 61, 95

Watkins L. L. et al., 2009, MNRAS, 398, 1757

Wegg C., Gerhard O., Bieth M., 2019, MNRAS, 485, 3296

Wetzel A. R., Hopkins P. F., Kim J.-h., Faucher-Giguère C.-A., Kereš D., Quataert E., 2016, ApJ, 827, L23

Xue X.-X. et al., 2014, ApJ, 784, 170

Yanny B. et al., 2009, AJ, 137, 4377

Zhao G., Zhao Y., Chu Y., Jing Y., Deng L., 2012, preprint (arXiv:1206.3569)

Zinn J. C., Pinsonneault M. H., Huber D., Stello D., 2019, ApJ, 878, 136

Zolotov A., Willman B., Brooks A. M., Governato F., Brook C. B., Hogg D. W., Quinn T., Stinson G., 2009, ApJ, 702, 1058

Zubovas K., King A. R., 2014, MNRAS, 439, 400

Zubovas K., Nayakshin S., Sazonov S., Sunyaev R., 2013, MNRAS, 431, 793

This paper has been typeset from a TEX/LATEX file prepared by the author.